**UNIVERSITÀ DEGLI STUDI
DI MODENA E REGGIO EMILIA**

Ph.D. Course in
*INFORMATION AND COMMUNICATION TECHNOLOGIES
(ICT)*

XXX Cycle

ENERGY HARVESTING AND SENSOR SYSTEMS EXPLOITING HETEROGENEOUS TECHNOLOGIES

Author:
MARCO LASAGNI

Tutor:
Prof. PAOLO PAVAN

Ph. D. School Director
Prof. SONIA BERGAMASCHI

Table of Contents

List of Figures

List of Table

List of Acronyms

IIoT: Industrial Internet of Things

ULP: Ultra Low Power

WSN: Wireless Sensor Network

EH: Energy Harvesting

IC: Integrated Circuit

CM-TED: Contact-Mode Tribo-Electric Devices

V-Q-x: Voltage-Charge-displacement relationship

TEG: Thermo-Electric Generator

DC-DC: Voltage Converter

ULVO: Ultra-Low Voltage Oscillator

CPR: Charge-Pump and Rectifier

LDO: Low-DropOut regulator

VBO: Voltage Biased Oscillator

FW-CPR: Full-Wave Charge Pump and Rectifier

nMOS: MOS transistor on n substrate

TEF: TriboElectric Flowmeter

ECS: Eddy Current Sensor

Introduction

THIS work describes the main results achieved by the author during his Ph. D., in the XXX Course of the International Doctorate School in Information and Communication Technologies of the "Università degli Studi di Modena e Reggio Emilia".

The continuous demand of new smart sensing solutions has opened the doors to new research activities aiming at overcoming one of the main drawbacks of conventional stand-alone battery powered wireless sensors: *the limited battery capacity*. Indeed, despite the availability of ultra-low-power electronic devices prolongs battery lifetime, the limited power source of battery is still a severe issue. Moreover, the high maintenance and replacement costs of the batteries, along with their sometimes impractical or difficult accessibility, are limiting factors to emerging scenarios such as Industrial Internet of Things (IIoT) and Industry 4.0. The current ambition is to combine artificial intelligence, smart sensing and smart actuation together with the ultimate goal to create smart factories able to enable robust consistent and accurate automation. In these systems each sensor node is autonomous, in term of electrical and computing powers, and able to compute, to promptly react to events, and to communicate through wireless links with other smart devices. In this scenario the continuous availability of autonomous wireless sensors play a crucial role, and therefore a wireless autonomous sensor powered by an unlimited power source is a necessity. Following this request, in parallel to the development of ever-lower power consumption devices, new green

and free energy sources, such as thermal mechanical energy, have been investigated as alternative power supplies to the batteries. This green and free energy can be harvested from the environment exploiting different Energy Harvesting (EH) technologies.

Particularly interested in the Energy Harvesting challenge, the Ph. D. candidate has been involved in a research project concerning the analysis, the development and the implementation of Energy Harvesting (EH) Systems developed for Wireless Sensors Networks (WSNs) and IIoT devices. In this perspective, a new generation of sensor systems capable of collecting energy from environmental energy sources (e.g. mechanical or thermal energies) has been developed to increase sensor lifetime with the ultimate goal to create autonomous sensors capable of operating for an arbitrary long time.

In particular, the research activity conducted by the candidate is threefold.

Firstly, he has worked on the development of transducers which exploit the triboelectricity effect to harvest energy from mechanical vibrations; this effect has also be exploited to create sensor capable of measuring the flow rate of gases and fluids.

Secondly, he has designed and realized an ultra-low voltage DC-DC converter, which exploits low thermal gradient EH.

Finally, he has designed and realized an ultra-low voltage and power inductive proximity sensor for ultra-low power sensor applications.

The work hereby presented is organized in five chapters.

Chapter I provides an overview of the nowadays Energy Harvesting

technologies, with particular emphasis on the two exploited energy sources: vibrational and thermal.

Chapter II describes the key concepts useful to understand how it is possible to convert the mechanical energy into electrical energy exploiting the triboelectric effect. Moreover, the first part of the author's research project will be presented. In particular, it concerns the development of Contact-Mode TriboElectric Devices (CM-TEDs) as mechanical energy transducer. The realized CM-TEDs consist of extremely low-cost commercial silicone used as dielectric material. In order to maximize the device performance, a simulation-aided custom design allows us to take into account application-dependent parameters such as the impact forces. This simulation model allows us to better understand the physics behind the contact-mode-triboelectric generation and also to infer a relationship between the generated current and the external forces acting on the system. This eventually allows us to predict the electrical performances of the device including their dependence on the impact force, thereby overcoming the limits of the classic models.

Chapter III presents an ultra-low-voltage DC-DC Boost converter for low thermal energy harvesting. The converter is designed to have a self-startup voltage of 11mV enabling very low Thermo-Electric Generator (TEG)-based applications. After a theoretical analysis and a simulation-aided design optimization the realized DC-DC converter improves its performances in terms of both self-startup voltage and low-voltage efficiency, as demonstrated by the comparison with other similar devices presented in literature.

Chapter IV is divided in two Sections which propose two different sensors exploiting different technologies. Section 4.1 describes an autonomous ultra-low cost triboelectric transducer capable of measuring the flow rate of gases and fluids. The realized device is extremely low cost because it uses commercial silicone as triboelectric material. The comparison between the performance of commercial Hall effect-based mechanical flow meters and our prototype, demonstrates the effectiveness of the proposed solution in both constant- and variable-flow conditions.

Section 4.2 proposes an ultra-low voltage and power proximity sensors based on eddy current principle. The sensor enabling circuit, based on a Pierce oscillator topology, is designed to turn on with low-voltage supply. The circuit has been optimized through the developed small-signal analysis and spice-simulation-aid. The measurements carried out on the realized prototypes show as it is possible to obtain a displacement resolution lower than 10μm with a power consumption lower than 30μW.

Finally, Chapter V summarizes the results obtained in this thesis work with particular emphasis on the author's contributions.

Chapter I
Energy Harvesting Sources

The purpose of Energy Harvesting (EH) is to collect green and free energy from the environment exploiting different transduction mechanisms, such as electro-mechanical, electro-thermal, etc., to provide electrical power for electronic devices.

In the WSN or IIoT scenario the intention of EH is to power directly wireless sensor nodes or to re-charge their battery equipment. Powering a wireless and remote sensor node harvesting energy from its operating environment, represents a zero-cost solution to prolong the battery lifetime. When battery replacement or maintenance is costly or dangerous, due to the practical inaccessibility to their operating ambient, EH represents the main attractive and alternative power sources. The constantly growing research field in EH solutions is driven by three main aspects:

i)   The possibility to enhance the battery lifetime and consequently reduce the maintenance and replacement batteries costs for WSNs,

ii) the possibility to reduce the pollution related to the battery production and disposal,

iii) searching for renewable and green energy resources with reduced carbon emissions.

Light, vibrational, thermal and radiofrequency are the most promising

energy sources. Table I.1 shows their approximate area power densities. High efficiency power conversion circuits are needed to avoid the wasting of the low energy available. The power provided by the four EH sources is at the same order of magnitude that an optimized ultra-low power (ULP) circuits typically consumes. Each of the four energy sources listed in the table present some challenges to consider.

Energy Source	Environment	Harvested Area Power density	Challenges
LIGHT	Indoor	$10\mu W/cm^2$	Wide Input Voltage range
	Outdoor	$10mW/cm^2$	
VIBRATIONAL	Human	$4\mu W/cm^2$	Vibrational Frequency Variability
	Industry	$100\mu W/cm^2$	
THERMAL	Human	$20\mu W/cm^2$	Low Output Voltage for Small Thermal Gradient
	Industry	$10mW/cm^2$	Efficient Heat Sinking
RADIO FREQUENCY	GSM	$0.1\mu W/cm^2$	Coupling and Rectification
	WiFi	$0.001\mu W/cm^2$	

TABLE I.1 POWER DENSITY OF THE MAIN ENERGY HARVESTING SOURCES [1]

We focus our attention on vibrational and thermal sources, which will be exploited and discussed in details in the following sections.

Vibrational energy can be found almost anywhere. Thus, converting mechanical energy from ambient vibrations into electrical energy is an attractive approach for powering Ultra-Low Power (ULP) devices. The state-of-the-art mechanisms of vibrational EH, i.e. piezoelectric EH, have the drawbacks to be high frequency selective[2][3]. The very narrow

working bandwidth leads to low conversion efficiency and low output power in environment with wide frequency spectrum, making the traditional mechanisms inefficient [4]. In this perspective a new research field, related to mechanical EH, is growing: triboelectric EH. Relying on a coupling effect of contact electrification and electrostatic induction the triboelectric principle has the potential to boost the vibrational energy harvesting [5][6][7] and self-powered sensing. By contacting two dissimilar materials, two opposite sign electrostatic charges are created on their surfaces. Consequently, if the surfaces are separated, a voltage difference can be established driving electrons in a closed circuit. The Triboelectric Energy Harvesting Devices (TEHDs) are widely used as a simple and low-cost vibrational and impact energy harvester, especially in the low-frequency range [5][7].

Apart from light and vibrations, thermoelectric conversion is the third important source for EH, that seem to be promising solutions to harvest some waste heat coming from industry processes or central heating systems. In recent years a lot of works were oriented to analyzing efficiency of thermal energy conversion into electrical one [8] and the physical structure of ThermoElectric Generators (TEGs) [9]. TEGs suffer from relatively low conversion efficiency (not exceeding 12%). The core element of a TEG is the thermocouple, that is comprised of two pillars, made of two different materials and a metallic interconnect, as shown in Figure I.1a. Each thermocouple converts the temperature difference, between the hot and the cold junctions, into a voltage by exploiting the Seebeck effect. A large number of thermocouples, connected thermally in parallel and electrically in series, forms a thermopile, as shown in see

Figure I.1b.

(a)   (b)
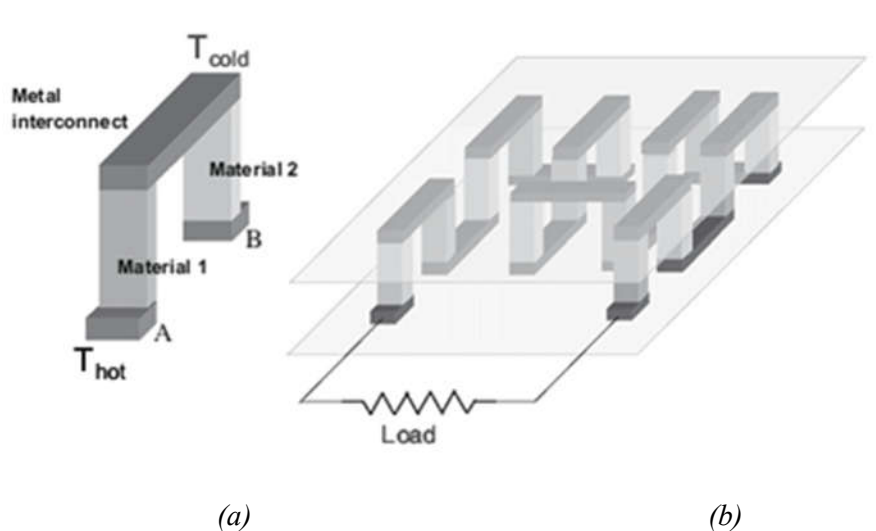
Figure I.1 Schematics of a thermocouple (a) and of a thermophile (b)[11]

Thermal gradients across a conductive material cause heat to flow. This results in mobile high-energy carriers flowing from high- to low-concentration regions and in a potential difference between the hot and the cold junctions. The reverse of this phenomenon, known as the Peltier effect, produces a temperature differential starting from an applied voltage. This is typically used in thermoelectric coolers (TECs). The polarity of the output voltage depends on the direction of the temperature difference across the TEG. By reversing the hot and the cold sides of a TEG, the output voltage changes its polarity. The generated DC-voltage and hence the generated power are proportional to the temperature gradient between the hot and the cold junctions, ΔT, and by the Seebeck coefficient of the two thermoelectric materials. Therefore a reliable electro-thermal model of a Peltier module is composed by a DC-voltage

source and the series resistance of the thermocouples [10][11].

Nowadays, TEGs are becoming more and more popular again as their prices are going down and the new potential applications have appeared due to recent developments in ever-lower electronic and wireless devices.

The commercial TEG, with an active area of 40x40mm, can generate voltages above 20mV by exploiting thermal gradient lower than 2°C [12]. Large thermal gradients are necessary to produce voltage and power levels suitable for practical applications, e.g. powering a sensor node.

Low power integrated circuits, like microcontrollers, transceivers, are commonly available for several years. Thus, the efforts are focused nowadays especially on ultra-low voltage conversion, energy storing and efficient power management. The best commercial integrated DC/DC converter is the LT3108-09 manufactured by Linear[13]. It is ideal for harvesting and managing surplus energy, and it operates with input voltages as low as 20mV. This voltage threshold represents the minimum start-up condition of the state of art converters. A key concern, when designing a TEG-based DC-DC converter for EH purpose, are the start-up voltage threshold and the efficiency of the converter.

Chapter II
Energy Harvesting Exploiting Triboelectric Effect

Among the large variety of energy sources, harvesting energy is widely considered an interesting option to prolong batteries lifetime for a wide range of applications including mobile/IoT devices and wireless sensor networks. Mechanical energy can be harvested by exploiting different physical principles, e.g. electrostatic, electromagnetic, piezoelectric, and triboelectric effects. Among all, the triboelectric effect has recently drawn a lot of attention in the scientific community because of its multiple advantages: broadband behavior suitable for collecting vibrations available in the environment, high energy density and easy fabrication process based on low-cost materials.

The tribo-electricity effect has been widely explored for its great potential to harvest mechanical energy from shocks and friction. Compared to piezoelectric, electrostatic and electromagnetic energy harvesting solutions, tribo-electricity generators offer great advantages in terms of broadband behavior. In addition, tribo-generators can be fabricated using low-cost organic materials that can deposited using very simple techniques, making this energy harvesting technology solution attractive for embedded applications, such as sensors systems [14][15].

The operating principle of tribo-electricity generators is based on the charge transfer between two materials that get in temporary contact.

Despite the intense research, the physical mechanisms and the charge species (i.e. electrons, ions or protons) involved in the contact electrification are not yet assessed completely. Nevertheless, it is clear that the charge transfer depends on the acidity (basicity) of the material, which affects its capability to attract electrons (protons) to form a base upon the contact. In addition, the electron transfer depends also on the bulk material properties[16]-[20].

The operating principle of Contact-Mode Tribo-Electric Devices (CM-TEDs) is based on the combination of contact electrification and electrostatic induction, [21]. In CM-TEDs tribo-electricity is generated when two different materials are put in contact. Due to the consequent charge transfer, electrostatic induction drives an electric current.

Several works presented in the literature demonstrated empirically that CM-TEDs could be used as energy sources as well as sensors. Most of the CM-TEDs developed for energy harvesting purposes, exploit the well-known cantilever shape (e.g. [22]). This kind of mechanical structure, originally used in pure piezoelectric energy harvesting systems, has been recently adopted also for hybrid piezo-tribo-electric devices (e.g. [23]-[25]). From a mechanical point of view, it is easy to realize devices with a cantilever shape, but these devices show an important limitation, i.e. their intrinsic narrowband behavior. Indeed, these devices present appreciable deformations (i.e. appreciable amount of generated energy) only in case of vibrations occurring at their own mechanical resonance frequency. From a practical point of view, this makes these devices not suitable for most of the real operating scenarios, where intensity and frequency of vibrations are randomly distributed and not known a priori. Therefore,

many efforts have been made to find solutions able to broaden the operating bandwidth of these devices. One of the most investigated solutions relies on the introduction of an amplitude limiter to induce non-linearity resulting in a broadband behavior of the device [22].This mechanism is particularly suitable for hybrid piezo-tribo-electric energy harvesting devices because, while the cantilever can be realized using piezoelectric materials (e.g. PVDF), a layer of tribo-electric material (e.g. PDMS) can be fixed to the free end of the cantilever and another one can be fixed to the amplitude limiter. The result is a classic piezoelectric transducer that operates in combination with a CM-TED. Another way to broaden the operating bandwidth in piezo-tribo-electric energy harvesting devices is the contact-separation mechanism of tribo-electric layers to induce stiffening in the cantilever as proposed in [26]. Of course, the hybridization of two mechanisms makes sense only if they are able to cooperate without any destructive interaction as shown in [27], where a combined tribo-electromagnetic energy harvester is presented.

As mentioned before, another research topic that is collecting a growing interest is the use of CM-TEDs to realize sensors (e.g. pressure sensors) for motion and posture tracking applications (e.g. [28]-[30]), or haptics (e.g. [31]).

Concerning the tribo-electric materials, most of the solutions presented in the literature exploit classic materials like PDMS or PET, while EVA is used in very few cases (e.g. [32]), nevertheless its advantages in terms of cost, flexibility, and biocompatibility. Moreover, EVA is available in form of sheets with macro-patterned bumps that increase the roughness of the surface allowing increasing the surface charge density and

consequently the tribo-electric energy harvesting capabilities, as demonstrated in several papers (e.g. [32]-[34]).

Concerning the physical dimensions of the CM-TEDs, instead, most of the solutions proposed in the literature are related to micro or nano-scale devices, while large area devices have been proposed only in the very recent past.

In this scenario, the contributions of the research activity proposed in this section are summarized hereafter.

First, in Section 2.1, the use of commercial silicone, as the material for the active layers in CM-TEDs, is proposed. This allows realizing large-scale devices at extremely low costs. Moreover, since the silicone is in form of gel when deposited on the electric contacts of the CM-TEDs, there is no need for additional manufacturing process steps for nano-structured patterning of bumps to increase the surface charge density due to the increase of its roughness during the solidification of the free surface. Realized samples were characterized using an ad-hoc test bench.

In order to maximize device performances, a simulation aided custom design is needed to explore different options for device optimization. For this reason, in Section 2.2, a CM-TED model that takes explicitly into account other application dependent parameters like the effect of the impact force between the active layers is presented. This model, validated by means of measurements performed on low-cost silicone-based CM-TED prototypes, allows understanding the contact-mode tribo-electric generation operating principles and their dependence on the impact force while predicting correctly the electrical performances.

2.1 Low-Cost CM-TEDs for Energy Harvesting

We exploit the above mentioned principles to implement prototypical tribo-electric mechanical energy harvester devices capable to generate high voltage and power using different combination of low-cost materials such as acetic, neutral and acrylic silicone. Realized samples were characterized using an ad-hoc test bench, which allows measuring device performances under either shock or periodic mechanical stimuli.

2.1.1   Tribo-electric devices and experimental set-up

Tribo-electric energy harvesting devices were realized through an easy in-house fabrication tool for the manual deposition of silicone in form of gel. After the deposition, the devices have been let at room temperature to solidify for 24 hours before the use in the tests. The simple structure of the devices is shown in Figure II.1. It resembles a Metal-Insulator-Metal (MIM) with two dielectric layers. All devices have the same 37x37mm active area, A, while they differs in the stack for contacts (C_1 and C_2), thickness (d_1 and d_2) and type of dielectrics (*dielectric$_1$* and *dielectric$_2$*) used. With reference to the device stack schematized in Figure II.1, the different performed tests and the relative parameters are summarized in Table II.1
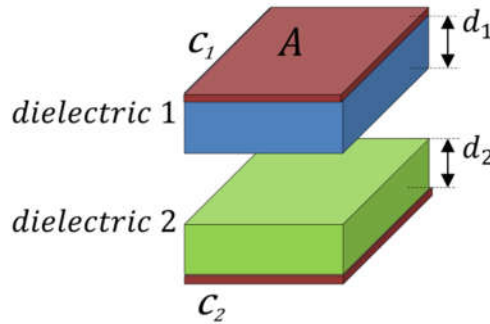
Figure II.1 CM-TED structure. Composition, contacts and thicknesses are listed in Table II.1.

As shown in Table II.1, the considered electrodes are made of Cu or Al, while different type of silicone, with different thicknesses, are used to compose the device stack. The different combinations highlighted in Table II.1 have been used to find the better combination of contacts and dielectrics (i.e. silicones) in terms of power generation.

Stack	Structure Stack
Stack	C_1	*dielectric$_1$*	d_1 *[mm]*	*dielectric$_2$*	d_2 *[mm]*	C_2
A	Cu	acetic	3	acrylic	3	Cu
B	Cu	neutral	3	acrylic	3	Cu
C	Cu	acetic	3	neutral	3	Cu
D	Cu	acetic	9	acrylic	3	Cu
E	Al	acetic	3	acrylic	3	Al
F	Cu	acetic	3	acrylic	3	Al

TABLE II.1 LIST OF THE TEST STRUCTURES WITH DIFFERENT THICKNESSES AND ELECTRODE/DIELECTRIC MATERIAL COMBINATIONS

Figure II.2 shows the experimental ad-hoc set-up implemented for the characterization of the devices. A K2007E01 electromagnetic shaker from

Modal Shop inc. has been controlled by an ad-hoc sinusoidal signal generated in order to guarantee both a very repetitive movement of the two plates of the device toward each other and a constant contact force, F. The frequency of the generated mechanical stimulus has been fixed to 20 Hz in all tests, while the contact force has been varied modulating the amplitude of the stimulus. In every test, the distance between the two dielectric layers of the device ranges from 0mm to 6mm upon the sinusoidal displacement applied by the shaker. The contact force F has been measured by means of an impact hammer (i.e. 086C03 from PCB Piezotronics), while the acceleration imposed by the shaker have been measured by a 352C41 mono-axial accelerometer from PCB Piezotronics). Both force and acceleration data have been acquired through a NI-cRIO-9233 acquisition board and a NI-USB9162 high speed USB carrier. The acquired data have been processed in real time by the Signal Express tool available for the LabVIEW software from National Instruments. The output voltage generated by the harvester has been measured with a DSO-X 3034A oscilloscope from Agilent Technologies.
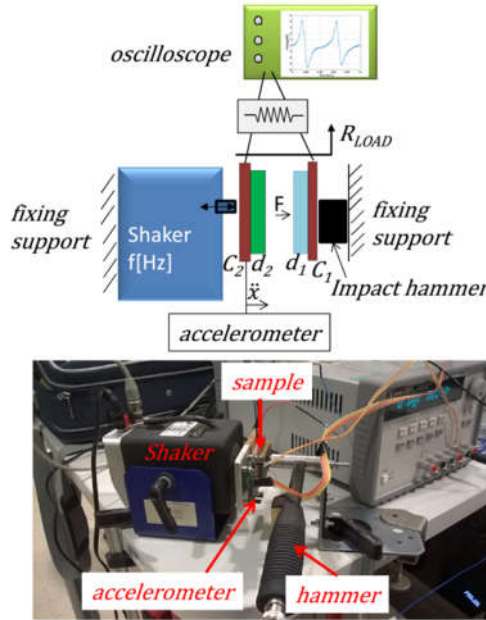
Figure II.2 Measurements setup. Simplified block diagram (top) and picture of the implemented test bench (bottom).

2.1.2   *Results and discussion*

Device performances were measured by analyzing both voltage and the power generation under different sets of stimuli. We characterized the tribo-electric harvester prototypes by measuring the output voltage and power in two different conditions:

- variable contact force, while keeping constant the load impedance (in the most of the cases we considered the 10MΩ input impedance of the oscilloscope probe);

- variable load impedance, R_{LOAD}, while keeping constant the contact force at $F=10N$;

Figure II.3a shows the typical output voltage waveform obtained by

applying a sinusoidal mechanical stimulus to the triboelectric device. Surprisingly, the voltage peaks at more than 80V upon the application of a 10Nconstant force. In general, the voltage amplitude depends on the device characteristics (i.e. dielectric and electrode materials, thickness of the dielectric layers) and the contact force, which is related to the acceleration imposed by the shaker. When the two dielectric layers get in contact, as shown in Figure II.3b, the acceleration becomes negative due to the mechanical resistance opposed to the shaker movement, generating the contact force F which is measured using the impact hammer. The time interval where F is higher than the defined noise threshold (i.e. 300mN) is used to detect the initial and final contact times between the two dielectrics.
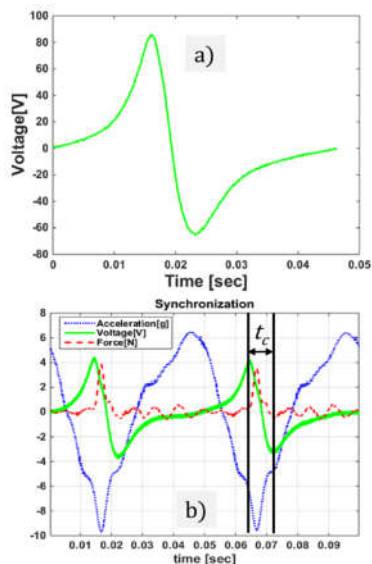
Figure II.3 Typical output voltage waveforms of the realized CM-TEDs. a) Output voltage waveform obtained with device stack A (see Table I) R_{LOAD} = 10MΩ and F = 10N; b) Synchronization of output voltage, F and acceleration (t_c is the contact time of the two dielectrics). All the three curves refers to the same vertical scale.

Figure II.4shows the output voltage generated by the device D (see Table II.1) when subjected to F =10N.It is interesting to note that the generated output voltage increases linearly with R_{LOAD}. This indicates that the optimum power matching between the harvester output and the load occurs for R_{LOAD} values higher than 50MΩ, which were not considered due to limitations of the available instrumentation.
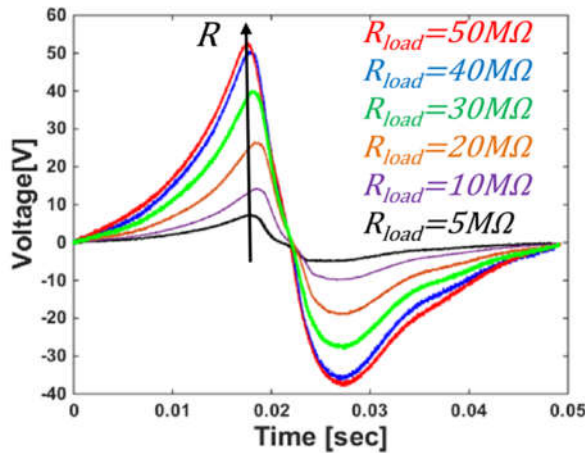
Figure II.4 Output voltage of the tribo-electric generator loaded with different R_{LOAD} at constant contact force F *= 10N.*

In order to characterize the performances of the realized harvester prototypes, we calculated the output power P_{OUT_MEAS}, as

$$P_{OUT\_MEAS} = \frac{1}{TZ_{LOAD}} \int_0^T V_{OUT\_MEAS}^2 (t)dt \qquad (1)$$

where V_{OUT_MEAS} is the output voltage across the load impedance imposed by the probe of the oscilloscope, Z_{LOAD} and $T=1/f$, f being the shaker frequency. For simplicity we considered only the resistive part of

the Z_{LOAD} , $R_{LOAD.}$

To identify the stack combination maximizing the output power, different silicone materials with the same thickness and the same electrodes were considered. Figure II.5 shows the output power generated by the A, B and C devices (Table II.1) connected to a 10MΩ load and subjected to a contact force F ranging from 1N to 10N. As expected, the acid-acrylic silicone combination (stack A) delivers the highest power, as the electron/proton charge transfer responsible for the contact electrification is maximum with materials with opposite pH characteristics.
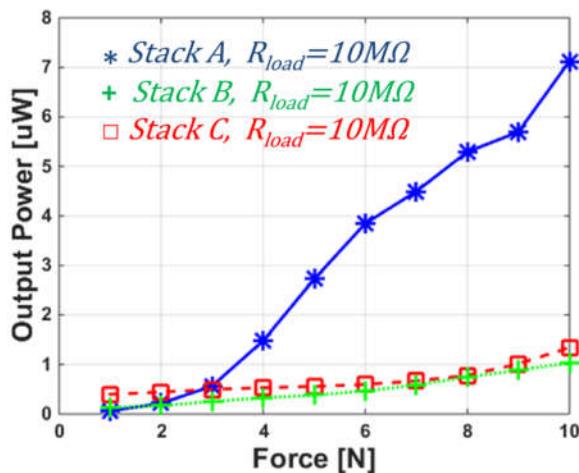
Figure II.5 Output power generated by the CM-TED connected to a 10MΩ load at different contact force, induced by different acceleration. We considered three devices with different combination of silicone dielectric material: stack A, B, C of Table I.

It is interesting to note that increasing the contact force leads to a larger output power, as expected. The dependence of the output power on the contact force is due to the "effectiveness" of the contact, which is affected by the surface roughness, whose effect reduces progressively by

increasing the contact force. Figure II.6and Figure II.7 show the output power generated by the tribo-electric device prototypes A and D (same electrodes and materials, different thickness) at increasing contact force and resistive load, respectively. The harvester with the acid-acrylic silicone material (that maximizes the output power) produces the largest output power when thinner dielectrics are used, independently of the contact force and of the load impedance. This is probably due to the higher capacitance, which maximizes the voltage for a given charge density, generated by the application of a given contact force. The equivalent capacitance between the two electrodes, is given by

$$C_{eq} = C_{d1} \parallel C_{d2} \parallel C_{air} \tag{2}$$

where $C_{d1}=A\varepsilon_l/d_1$ and $C_{d2}=A\varepsilon_l/d_2$ are the capacitances of the two dielectric layers, ε_n and d_n being the dielectric permittivity and the thickness of the *n-th* dielectric layer, respectively; $C_{air} = A\varepsilon_0/d_{air}$ is the capacitance of the air gap between the two dielectrics, ε_o and d_{air} the air dielectric constant and the thickness of the air gap, respectively.
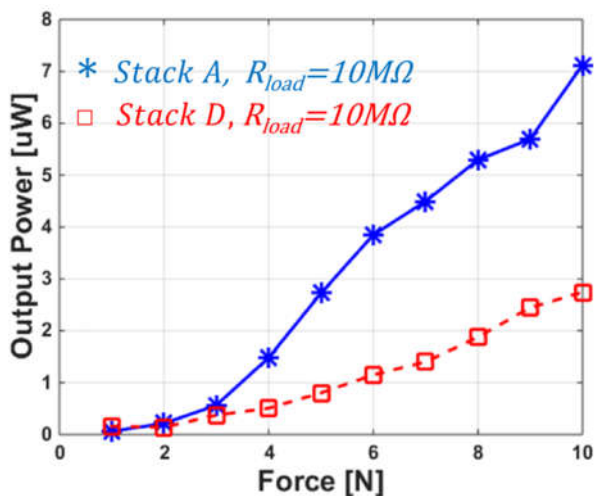
Figure II.6 Output power generated by the CM-TED connected to a 10MΩ load at different contact force, induced by different acceleration. We considered two devices with different thickness of silicone dielectric material: stack A and D of Table II.1.
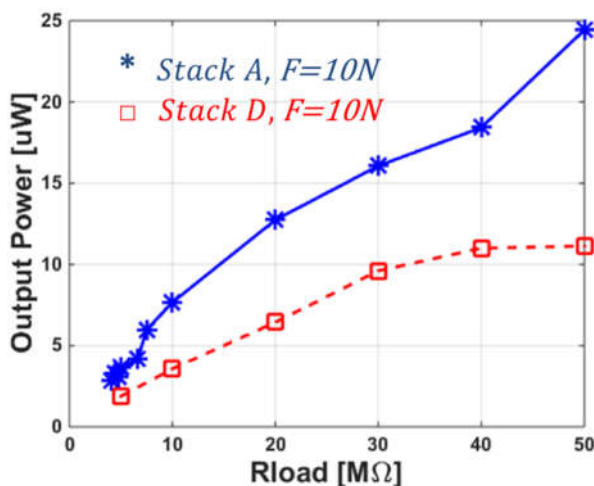
Figure II.7 Output power generated by the CM-TED connected to a variable load at contact force F = 10N. We considered two devices with different thickness of silicone dielectric material: stack A, and D of Table II.1

The CM-TED can be modeled with a Thévenin equivalent circuit comprised of a voltage generator, which models the open-circuit voltage

V_{oc}, connected in series with the impedance given by(3). Noticeably, V_{oc} is dependent on the tribo-electric charge generated by both the contact electrification and the variable capacitance of the air gap between the two dielectrics. The voltage generated by the device when a load is connected, V, is given by

$$V = V_{oc} - \frac{Q}{C_{eq}}$$ (3)

where Q is the transferred charges from one electrode to the other[1]. Since the dielectric capacitance is inversely proportional to the dielectric thickness, the voltage V generated by the tribo-electric device increases with the reduction of the dielectric thickness, according to(3),consistently with the trend shown in Figure II.6and Figure II.7.This is due to the higher equivalent capacitance C_{eq}, which minimizes the second term Q/C_{eq} in (3). Similarly, increasing (decreasing) the distance between the two dielectric layers modifies the air capacitor C_{air}, changing the voltage according to (3)due to a pure electrostatic effect.

At the same time, also the electrode material influences the output power generated by the harvester. In this respect, Figure II.8 shows the output power generated by A, E and F devices, when subjected to a constant contact force F = 10N and connected to a variable load R_{LOAD}. The device with both contacts made in aluminum (stack E) shows the best performance in terms of generated output power for the lowest R_{LOAD}. On the contrary, the device with the electrodes made of copper shows the highest power at the highest R_{LOAD}.

On the contrary, the device with the electrodes made of copper shows

the highest power at the highest RLOAD.
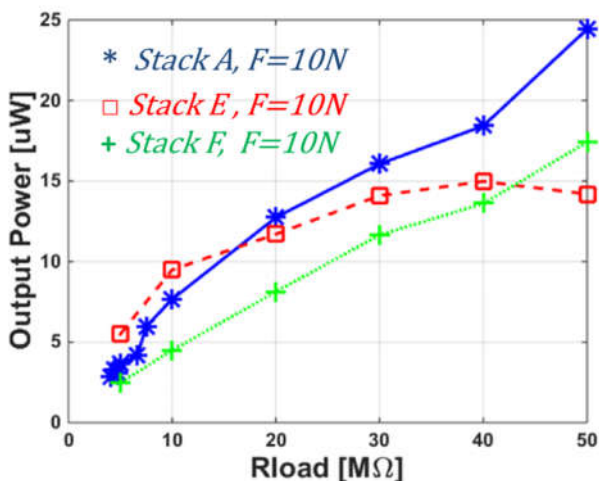
Figure II.8 Output power generated by the CM-TED connected to a variable load at contact force F *= 10N. We considered three devices with different combination of contact material: stack A, E and F of Table II.1.*

2.1.3   Conclusions

In this section a CM-TED designed to harvest energy from mechanical shock has been presented. Device prototypes, realized using an in-house fabrication process, were fabricated using ultra-low cost organic materials such as silicone. The different combinations of silicone were investigated to identify the best structure in terms of power generation. Measurements carried out on the device prototypes show a 25µW output power peak for a device subjected to 10N contact force loaded with a 50 MΩ impedance.

2.2 Modeling of Low-Cost CM-TEDs

In this section we investigate the effect of the contact force in Contact-Mode TriboElectric Devices (CM-TED). In this kind of devices, as shown in the Section 2.1, the generated output voltage and the electrical energy harvested from mechanical impacts depend on the contact force. The number of impacts and the contact force influences also the surface charge density of the triboelectric layers of CM-TED. This is confirmed by the measurements carried out on the low-cost CM-TED prototypes we realized using commercial silicone as triboelectric material. The effect of the impact force has been included into a device model suitable for both dielectric-to-dielectric and contact-to-dielectric triboelectric devices.

In particular, the developed model allows the estimation of the surface charge density of the dielectric materials used in the CM-TED. While in the classic models, e.g. [21], it is considered constant and dependent only on material properties, in the proposed one it is demonstrated to be a function of the impact force. This represents an important improvement compared to models proposed for the CM-TED up to now in the literature, which neglect the effect of the impact force.

The model predicts the output voltage and power at given conditions and it can be used to design ultra-low cost triboelectric energy harvesters.

In addition, the model equations allow also to estimate the impact force required to obtain a given output voltage accordingly with the voltage/power requirements of a specific application. Consequently, the developed model can be used to design custom CM-TED, for both energy harvesting and sensing purposes.

2.2.1   *CM-TED Prototypes, Measurement Set-up, and Experimental Results*

The CM-TED can be classified in dielectric-to-dielectric and contact-to-dielectric devices. As shown in Figure II.9 they differ only in the number of dielectrics acting as triboelectric layers. From a device modeling point of view the most general representation is related to the dielectric-to-dielectric device (Figure II.9a), therefore this is the one we considered in the model development. The representation of the device sketched in Figure II.9b, indeed, can be easily obtained by means of a simplification of the model obtained for devices with the structure shown in Figure II.9a.

The CM-TED prototypes we fabricated and used to develop and test the model have the dielectric-to-dielectric structure shown in Figure II.9a, where the Dielectric 1 is Acrylic Silicone (with $\varepsilon_{r1} = \varepsilon_{acry} = 10$, and thickness $d_1 = 1.9$ mm) and the Dielectric 2 is Acetylic Silicone (with $\varepsilon_{r2} = \varepsilon_{acet} = 2.2$, and thickness $d_2 = 1.9$ mm). Two classic FR4 boards for PCB applications with 35 μm Cu layer have been used as Contact 1 and Contact 2. The device prototypes were realized using a very simple and low-cost in-house fabrication process: the silicone-gel dielectrics are manually deposited at room temperature, and they are let solidifying for 24 hours. The obtained device has an active triboelectric area, *S,* of 37x35 mm.
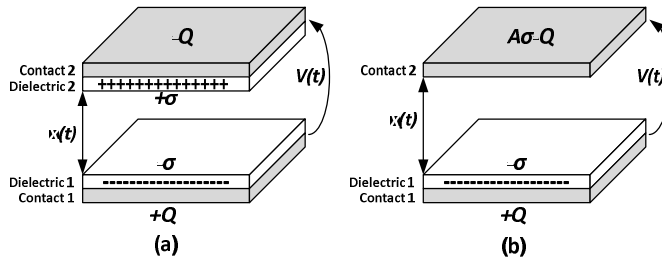
Figure II.9 General structures of Contact-Mode Triboelectric Energy Harvesting Devices. (a) Dielectric-to-Dielectric, (b) Contact-to-Dielectric.

The realized CM-TED has been characterized exploiting the setup shown in Figure II.10. It comprised of a laser vibro-meter, an electromagnetic shaker, an instrumented impact hammer and an oscilloscope. For each test, this set-up allowed to measure: *i*) the output voltage generated by the CM-TED when the two tribo-electric layers (i.e. the two dielectric layers) are repetitively put in contact with a given force; ii) the relative displacement, the relative velocity and the impact force between the two dielectric layers of the CM-TED.
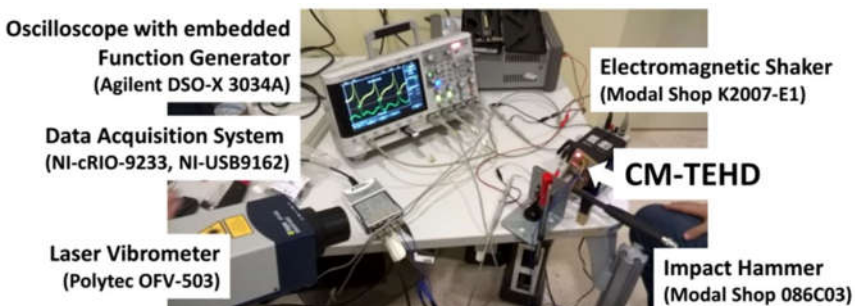
Figure II.10 Measurements Setup

In particular, the device plate of the CM-TED with the layer of Acrylic Silicone is fixed to the impact hammer, used to measure the contact force of the mobile plate of the device.

The mobile plate, with the Acetylic Silicone triboelectric layer, in turn, is fixed to an electromagnetic shaker (i.e. Modal Shop K2007-E1)to generate the mechanical stimulus with controlled frequency and amplitude.

The shaker is excited exploiting the waveform generator embedded in the oscilloscope (i.e. Agilent DSO-X 3034A) used to acquire the output voltage generated by the CM-TED.

Velocity and displacement of the CM-TEHD's mobile plate are measured by means of a laser vibrometer (i.e. Polytec OFV-503), while the force of the repetitive impacts is measured by the reference impact hammer (i.e. Modal Shop 086C03). All measured signals are acquired and processed in real time by a LabView-based data acquisition system comprised of a data acquisition board(i.e. NI-cRIO-9233) hosted by a single carrier module for USB interface (i.e. NI-USB9162) with a personal computer.

Figure II.11 shows three different output voltage waveforms generated by the CM-TED for three different peak impact forces (i.e. 12N, 25N, 50N respectively). Acquisitions are synchronized in post processing thanks to the velocity, displacement and contact force of the CM-TED mobile plate measured by the laser vibro-meter and the instrumented impact hammer. It is already possible to note that the contact force influences the voltage generated across the device terminals and

consequently the CM-TED generated output power.
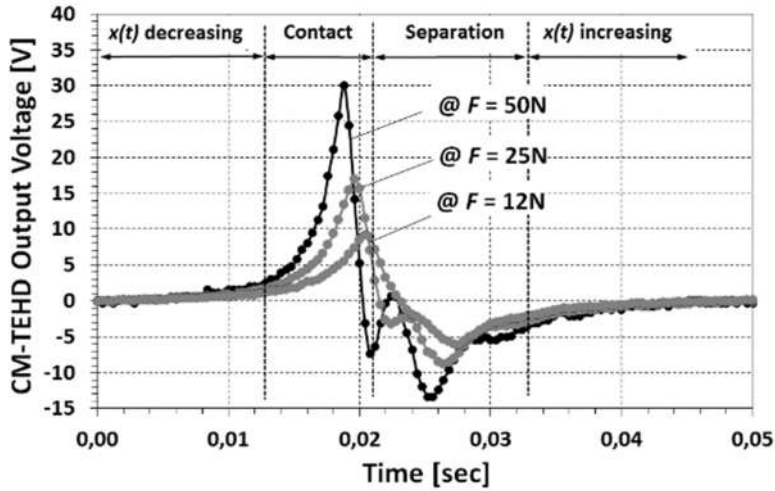
Figure II.11 Output voltage waveforms generated by the CM-TEHD at different forces. The waveforms are used as input of the developed Matlab-based model. The positive peak is larger than the negative one: this is due to the faster contact phase between the triboelectric layers than the separation one, while the total amount of charge transferred is the same.

2.2.2 *The Triboelectric Device Model Accounting for the Impact Force Effect*

In order to model the CM-TED devices including the contact force effect, we extended the popular models proposed in [21] for the operation and the power generation.

The most popular models proposed for the operation and the power generation modeling of a CM-TED are based on the so-called "*V-Q-x* relationship" (e.g. [21]), where *V* is the voltage generated between the two CM-TED contacts, *Q* is the amount of transferred charge between the

contacts, and x is the distance between the two CM-TED dielectric layers, that varies accordingly with the mechanical stimulus. According to this models, the voltage generated by the CM-TED device depends on the charge transferred and on the displacement as:

$$V = -\frac{Q}{S\varepsilon_0}\left(\frac{d_1}{\varepsilon_{r1}} + \frac{d_2}{\varepsilon_{r2}} + x(t)\right) + \frac{\sigma x(t)}{\varepsilon_0} \qquad (4)$$

where S is the active area of the CM-TEHD, ε_0 is the air dielectric constant, d_1 and ε_{r1} are the thickness and the relative permittivity of dielectric 1, d_2 and ε_{r2} are the thickness and the relative permittivity of dielectric 2, and σ is the constant surface charge density coefficient. Indeed, these models consider an instantaneous contact time and do not take into account the effect of the contact force F between the two dielectric layers, which was measured to influence the generated voltage (see Figure II.11).

Therefore, we included this effect by considering that the charge density σ depends not only on the properties of the dielectric materials but also on the contact force, i.e. $\sigma=f(F)$. This agrees with experimental results on triboelectric generators with specific surface structures (e.g. pyramid arrays) reported in the literature (e.g. [22],[35]).

Figure II.12 shows the surface charge density, σ, estimated using the experimental output voltage and output power measured during the characterization of the same CM-TED sample described in the previous section. The characterization has been carried out by exploiting the same setup shown in Figure II.10.
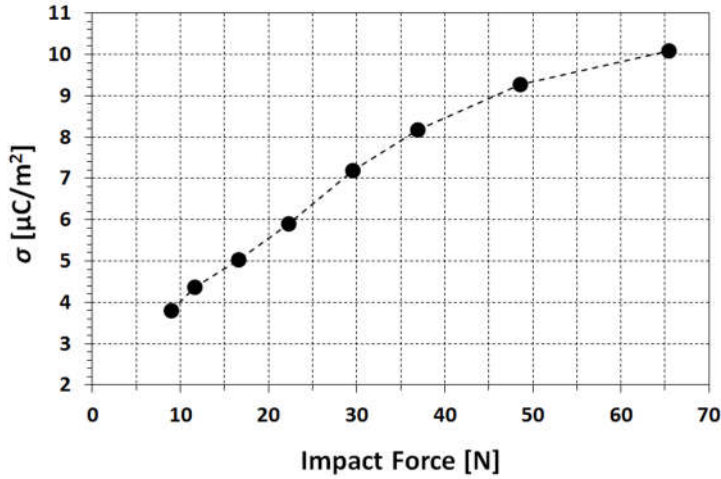
Figure II.12 Surface charge density values calculated by substituting in (1) the measured values of the CM-TED output voltage, $V_{OUT\_MEAS}(t)$, and displacement, $x_{MEAS}(t)$, for different values of impact forces F.

It is possible to note as the impact force F influences in a not negligible way the surface charge density σ, that passes from less than 4 $\mu C/m^2$ to more than 10 $\mu C/m^2$ in the considered range of F (i.e. 9 N ÷ 65 N).

For each considered F, the calculated value of σ has been obtained by applying to (4) the measured value of the CM-TED output voltage, $V_{OUT\_MEAS}(t)$, and the displacement, $x_{MEAS}(t)$.

In order to include the dependence of σ on the impact force, F, (i.e. $\sigma = \sigma(F)$) in the classic CM-TED models defined by (4), we developed a two-step procedure based on the measured values of the CM-TED output voltage, $V_{OUT\_MEAS}(t)$.

First, it is possible to calculate the measured output power of the CM-TED, P_{OUT_MEAS}, as in (1) by using the measured output voltage,

V_{OUT_MEAS}, and knowing the load impedance imposed by the probe of the oscilloscope, Z_{LOAD}, and the period T of the stimulus provided by the shaker (i.e. 50msec for the reported example).

Second, thanks to an ad-hoc developed automatic and iterative power fitting Matlab-based procedure, it is possible to find the optimal value of the surface charge, $\sigma_{OPT}(F)$, that minimize the output power error, $\varepsilon_{POUT}=$ P_{OUT_MEAS} - P_{OUT_SIM} for a given F, where P_{OUT_SIM} is the simulated output power calculated from the simulated output voltage V_{OUT_SIM}. In turn, V_{OUT_SIM} is obtained by applying the displacement measured by the vibrometer $x_{MEAS}(t)$ to (4) and varying iteratively the value of σ. The procedure has been repeated for all the considered impact forces F.

The expression used to define $\sigma_{OPT}(F)$ used in the procedure summarized above is reported in (5),

$$\sigma(F)|_{n\to\infty} = \sigma_\infty[1 - e^{-cF}] + \sigma_0 e^{-cF} \qquad (5)$$

where $\sigma(F)$ is the surface charge density, expressed in exponential form after a number of impacts, $n,$ large enough to approximate a steady state condition of the charge transfer mechanism at a given impact force, F, (i.e. $n \to_\infty$).In (5) σ_∞, σ_0 are the saturation and the initial value of the charge density for the considered dielectric materials, respectively, and c is a coefficient obtained from the automatic iterative calibration procedure implemented in the model.

The empirical relationship expressed by (5) has been obtained by applying to large-scale CM-TEDs the approach proposed in [37] to describe the tribo-electric charging mechanisms of single particles hitting a wall. In particular, we used the assumption of [37] concerning the

saturation of the amount of transferred charge, q, after a given number of impacts, n, and using the relation $q = \sigma S$, where S is the contact area of the CM-TED. The obtained $\sigma = f(F)$ can be directly included in (4) to account for the contribution of the impact force F on the output voltage V generated by the CM-TED, accordingly with the macroscopic behavior observed in the CM-TED prototypes.

Considering the device stack described in the previous section and the experimental output voltage waveforms shown in Figure II.11 as input parameters, the proposed model has been applied to the CM-TED prototype we realized. With reference to(5), the model produced (σ_∞, σ_0, c) = (12.3 $\mu C/m^2$, 1.69 $\mu C/m^2$, 0.02459) for the considered CM-TED. Using these values in (5) and including the resulting $\sigma(F)$ in (4) it is possible to estimate the CM-TED output voltage for any given impact force F.

Figure II.13 and Figure II.14 show respectively the comparison between the measured output voltage and the measured output power with the simulated ones obtained by applying the proposed model. A very good agreement between simulations and measurements is shown, supporting the validity of the proposed model. The results confirm that, differently from the assumptions of previous models, the contact time is not zero and the impact produces a variation of σ. This effect contributes also to the output power generation, which increases linearly with F (see Figure II.14).
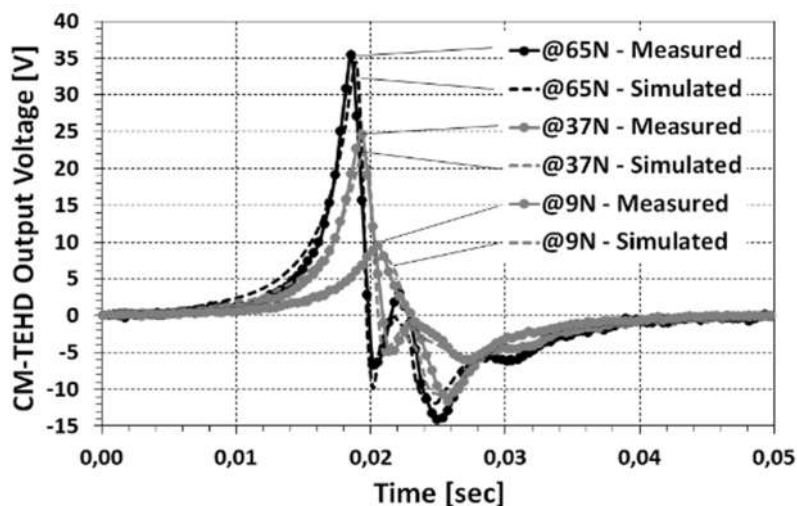
Figure II.13 Comparison between the measured output voltages generated by the implemented CM-TEHD prototype at 9N, 37N and 65N and the corresponding output voltages simulated by means of the proposed model.
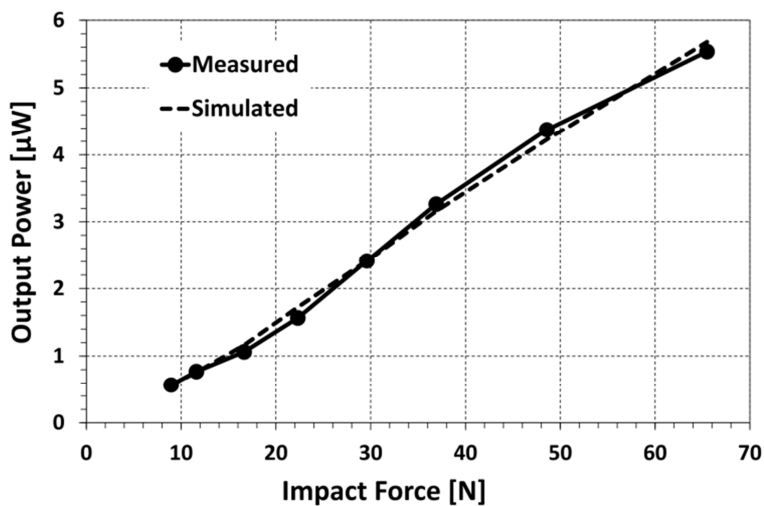
Figure II.14 Comparison between the output power of the implemented CM-TEHD prototype calculated from the measurements with a $Z_{LOAD}=10M\Omega//11pF$ (oscilloscope's probe) and the simulated ones. $P_{OUT} = \frac{1}{TZ_{LOAD}} \int_0^T V_{OUT}^2 (t)dt$, where T=50msec is the period of the stimulus provided by the shaker.

Finally, as already mentioned, the model can be used also to design custom CM-TEDs. To this purpose, we realized and characterized a second prototype with: i) same materials stack and same active area of the first one; ii) different thicknesses (d_1 = 3 mm for acrylic silicone, d_2 = 9 mm for acetylic silicone).

The surface charge density $\sigma(F)$, as well as the coefficients (σ_∞, σ_0, c), calculated by the model, are specific parameters for the considered materials pair put in contact. Therefore, they can be used also for the simulation of the second CM-TED prototype. An example of comparison between simulated and measured output voltage for the second CM-TED prototype in the case of a desired F = 9 N is shown in Figure II.15. Also in this case, it is possible to note the very good agreement between simulations and measurements, a further demonstration of the validity of the proposed solution. Comparing the results of Figure II.13 for F = 9 N and Figure II.15, it is possible to note as the second prototype generates a peak output voltage smaller than the first one. This is due to the effect of the thicker tribo-electric layers on the equivalent capacitance of the device, as already explained in the literature (e.g. [6]).

Of course, the effect of impact force F in the output voltage (and power) generation is valid also in the case of contact-to-dielectric devices (i.e. devices with only one tribo-electric layer, see Figure II.9b). For these devices (4) can be easily adapted by eliminating the terms ε_{r2}/d_2 related to the second dielectric layer.
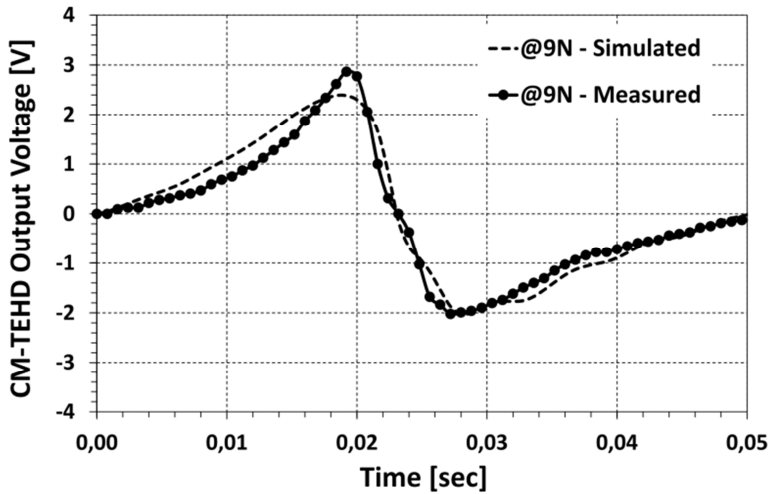
Figure II.15 An example of comparison between simulated and measured output voltages generated by the second CM-TEHD prototype for a desired F = 9N.

2.2.3   Discussion on influence of the impact force on the surface charge density

As demonstrated in several papers (e.g. [26], [32]-[34]) the output voltage generation takes benefit from a bumped micro nano-pattern designed on the surface of the tribo-electric layer of the CM-TED. Indeed, this produces an increase of the surface charge density σ of the layer and an increase of the contact area. Moreover, [37] demonstrated that σ depends also on the number of impacts n. In particular, σ increases with the number of consecutive impacts and saturates after a number of consecutive impacts large enough to reach a steady state condition of the tribo-electric layer surface.

As shown in the following, we demonstrated that the number of impacts n needed to reach the steady state condition depends on the impact force F.

In order to demonstrate the effect of F and n on σ in CM-TED large scale devices, we realized a 40x40 mm prototype of a CM-TED device with a 1 mm thickness of acetylic silicone acting as active tribo-electric layer. Differently from the other prototypes, the device has been realized using a fabrication process to reduce the surface roughness, minimizing the contribution of the increase of the contact area during the impact. In particular, the deposited silicone has been let solidify sandwiched between the FR4 board used as contact of the CM-TED and a grinded aluminum surface. The resulting roughness is the same of the aluminum surface that has been grinded with a standard mechanical machining (i.e. 0.8 µm).

The obtained prototype, resembling a contact-to-dielectric CM-TED (see Figure II.9b), has been tested in a range of low impact forces F (i.e. up to 25 N) allowing to further neglecting the contribution of the increasing contact area in the CM-TED output voltage generation during the impact.

Using the developed model, it has been possible to obtain the value of σ as function of the number of consecutive impacts for different values of F. The results are shown in Figure II.16. According to (5), Figure II.16 reveals that σ has an initial value σ_0 (i.e. for $n = 0$) that depends only on the specific triboelectric material considered.

The slight differences in the initial surface charge density σ_0 at different F are due to the differences of the initial of the single measurement carried out. Indeed, in the case of prolonged series of consecutive impacts, a residual charge remains trapped on the surface of the tribo-electric layer

due to drift, diffusion and charge recombination mechanisms.

The decay of this residual charge takes a relatively long time [38]. Consequently, with the available setup, it was quite difficult to determine when the residual charge was completely recombined allowing starting the new data acquisition with the same σ_0.
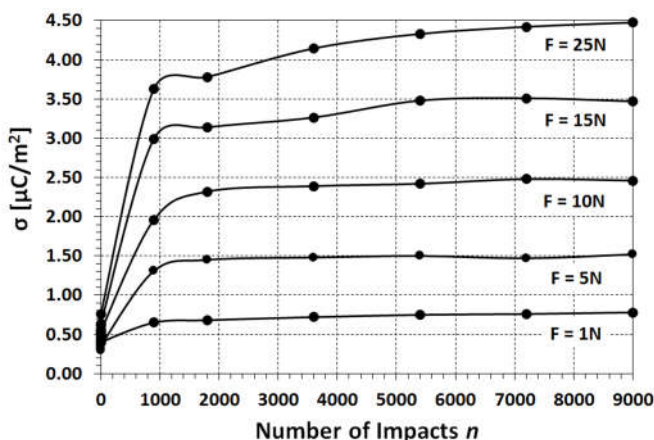
Figure II.16 Surface charge density, σ, vs. number of consecutive impacts, n, for different values of F. Each measurement have been carried out with periodic impacts at the frequency of 30 Hz, which is the excitation frequency of the shaker.

Indeed, if the impact frequency is high enough, a small amount of residual charge remains trapped on the surface of the triboelectric layer at each impact. Therefore, the larger is the measurement time (i.e. larger number of impacts) the larger is the time interval needed between two set of measurements.

For example, Figure II.17 shows the measured CM-TED output voltage, V_{OUT}, once a 3 minutes long series of repetitive impacts at the frequency of 30 Hz with a constant impact force $F = 10$ N has been stopped. In order to highlight the decay effect of the trapped residual charge and have a rough estimation of when the surface charge density

came back to its original value σ_0, we did not turn off the shaker. We kept the same frequency and reduced the amplitude of the vibration to the level needed to have no contact between the mobile plate of the shaker and the tribo-electric layer of the realized CM-TED (i.e. no impacts occuring).
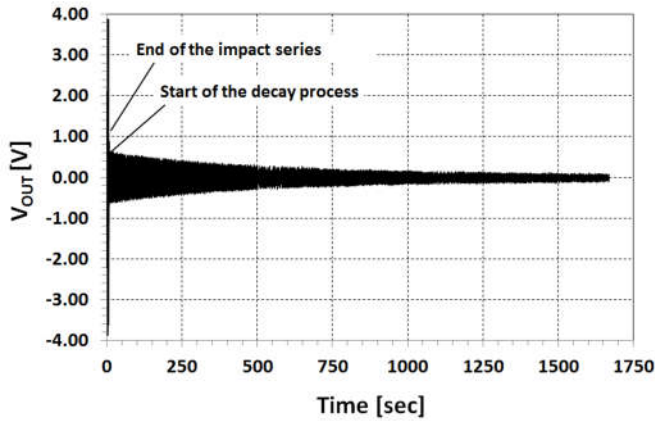
Figure II.17 Decay of the residual charge in case of 3 minutes long series of repetitive impacts. The impacts occurred at the frequency of 30 Hz, while the impact force was F = 10 N.

As one can note, once the impact series ends, there is an instantaneous drop of the output voltage generated by the CM-TED because the contribution of the impact force in the charge (and output voltage) generation ends. Keeping moving the mobile plate of the shaker allows the operation of the CM-TED, but due to the absence of impacts, the residual charge trapped in the tribo-electric layer of the device recombines in air. Consequently, the output voltage of the CM-TED decreases over the time to reach a steady state condition at the level corresponding to the specific working condition imposed by the movement of the mobile plate of the shaker, where the only contribution in the output voltage generation is due to the electrostatic induction.

The amount of trapped charge for each impact depends proportionally on the impact force F. Indeed, as it is possible to note in Figure II.16, this has a non-negligible effect on the number of impact n needed to reach a steady state condition of the surface charge density σ, as stated in [37]. For example, for the considered CM-TED, while in first approximation, σ can be considered quasi-constant after $n = 1800$ for $F = 1N$, σ can be considered quasi-constant after $n = 3500$ for $F = 10N$.

2.2.4   Conclusions

Concluding, we presented a model that can be used to design large scale CM-TEDs. Differently from the models presented previously in the literature, the proposed one takes into account the effect of the impact force.

In addition to the known effect of the number of impacts, indeed, the presented results demonstrate how also the impact force influences in a not negligible way the surface charge density, σ, of tribo-electric layers. Several prototypes of ultra-low cost silicone-based CM-TED has been realized to validate the model. As confirmed by the very good agreement between measurements and simulation results, the developed model predicts the output voltage and the output, power at given working conditions (e.g. estimated impact force, displacement, electrical load), and can be used to design CM-TEDs for energy harvesting purposes.

Chapter III

Ultra-Low Voltage Boost Converter for Low Thermal Gradient Energy Harvesting

In this chapter an enhanced self-powered ultra-low input voltage DC-DC converter is presented. The converter needs only 11mV input start-up voltage providing a 2.1V output voltage, while provides more than 3V output voltage with only 12 mV input voltage. It was optimized to work in the range 11mV-20mV. With 11mV input voltage the time needed to charge a completely discharged 500uF capacitor at 2.1V is about 524s. From an energy harvesting point of view, it represents an enabling functional block to convert the low voltage generated by the Thermo-Electric Generator (TEG) operating with a very low thermal gradient, lower than 1°C. In fact as the measurements demonstrate, the implemented circuit is able to convert thermal energy starting from a thermal gradient of 0.6°C by means of a commercial TEG having a thermal resistance of 2°C/W. The solution, tested with an input thermal range between 0.6 to 4°C, can support low-power pulsed-load applications, such as low duty cycled BLE transmission with transmit burst rate in the range 0.08 - 3.4Hz.

3.1 Introduction

The proliferation of Industrial Internet of Things (IIoT), such as smart wireless sensor for measurement and control, has been driven by the new ultra-low-power sensor nodes. Despite the reduction of power need, that has allowed battery lifetime extension, the limited power source of battery is still a severe issue and the main limiting factor of the emerging IIoT.

In this scenario, harvesting energy from environment can supplement or eliminate the need for batteries and all the correlated maintenance costs and problems when their accessibility is difficult or impractical. Ultra-low power sensor nodes combined with new energy harvesting technologies, can produce completely autonomous systems[39]. However, the limited power attainable from energy transducers leads us to search for increasingly efficient methods and circuits to manage and gather the energy. But since the energy available is often very small and unpredictable, most of the initial target applications can only work with a very constrained duty-cycle. This ensures sufficient time to accumulate energy, while a microprocessor or a sensor circuit is in sleepmode. This type of system needs to be in sleep mode and wake up only to perform its duty. Energy harvesting circuitry must be able to capture energy from sources producing less than 50mV. We are expecting an increasing demand of solutions using, for example, thermoelectric generators (TEGs) subject to very low thermal gradients.

Some recent publications [40] and [41] have reported TEG-based applications operating at supply voltages as low as 21 mV. [42] demonstrates energy harvesting from as low as 12-mV input while biased

by an external 1V battery. Previously published TEG-powered converters operating with the low minimum input voltage 9mV [43] are able to regulate a voltage at 1.2V. At this condition the output voltage is not sufficient to supply the traditional devices that require a voltage larger than 1.8V. However, they use DC-DC converters that require specific startup conditions. Moreover, in some of these publications, the real-startup voltage condition is not clearly presented and discussed.

The ignition of a DC-DC converter requires a time-varying signal, which is commonly obtained from an electronic oscillator. The current state-of-the-art seems to rely on low-voltage DC-DC converters operating at minimum 20mV [13], which impose a severe limitation to the maximum energy that can be harvested.

To cope with this, the research activity has focused on the possibility to overcome this limitation in order to reduce the minimum threshold for voltage conversion start-up. In order to achieve this result, a modification of the typical converter topologies was developed with the aim of reducing the minimum voltage required for start-up, as discussed in the Section 3.3. Minimizing the startup voltage results in a higher conversion efficiency.

This chapter is organized as follow. Section 3.2 presents an overview of the state-of-the-art and main limitations of the DC-DC converters for thermal energy harvesting applications. The proposed solution is deeply described in Section 3.3. Experimental results confirming the effectiveness of the proposed solution are presented in Section 3.4. Finally, Section 3.5 concludes the chapter.

3.2 Analysis of performances and limits of current low-voltage DC-DC converters

The current state-of-the-art relies on self-startup low-voltage DC-DC converter operating at minimum 20mV to produce at least 1.8V output voltage level, which impose a severe limitation to maximum energy that can be harvested. For low-voltage thermal energy harvesting with an input voltage in the range 20mV-50mV, the DC-DC converters commonly used and discussed in literature use an initial stage with a self-oscillating Armstrong architecture [44] as shown in Figure III.1, followed by a charge-pump and a rectifier.

The operating principle exploits the resonant LC-oscillator composed of a small step-up transformer (with N turns ratio) and a normally-on mosfet (M_{DEP}) to start the self-oscillation and to boost the low-input-voltage. The M_{DEP} mosfet is in charge of starting the oscillation and is commonly parallelized with an enhancement mosfet (M_{ENH}) that operates in switched-mode and in charge of the power transfer. In fact, once the circuit is turned on the oscillation gradually increases as soon as it reaches the threshold voltage of the M_{ENH} the circuit starts to operate in switched-mode. C_{GS}, C_k and C_L are respectively the gate-source capacitance, a capacitance between the transformer and the gate of the transistor and the input capacitance of the charge pump and rectifier.
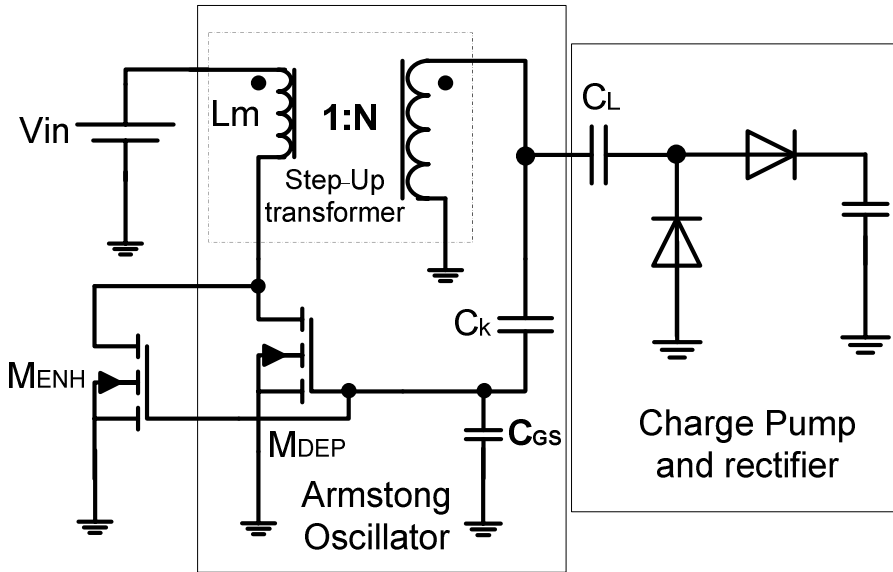
Figure III.1 Classic Armstrong oscillator with a charge-pump and rectifier.

Several works demonstrate that this kind of circuit has the main limitation to turn on with an input voltage higher than 20mV.

As widely discussed in literature the start-up condition of this topology oscillator occurs (neglecting in the C_1 and C_L), when

$$g_m(V_{gs(0)}, V_{ds(0)}) \, N \, r_{ds}(V_{gs(0)}, V_{ds(0)}) > 1 \tag{6}$$

where N is the transformer turns ratio, r_{ds} and g_m are respectively the channel resistance and the transconductance of the depletion mosfet at initial voltage, $V_{gs}(0)=0V$ and $V_{ds}(0)<V_{in}$.

A normally-on n-mos typically used are the BSP149 that exhibits a threshold voltage of -870mV [45]. Since $V_{gs} = 0V$, applying an input voltage at the primary side of the transformer lower than 50mV the mosfet works in the active region.

$$V_{ds(0)} < 50mV \ll |V_{th}| \tag{7}$$

Considering the level-1 mosfet equation allows calculating:

$$g_m = k'_n \frac{W}{L} V_{ds} \tag{8}$$

$$r_{ds} = \frac{1}{k'_n \frac{W}{L}(|V_{th}| - V_{ds})} \tag{9}$$

where k_n' is transconductance factor (i.e. electron mobility and oxide capacitance), W and L are respectively the width and length of the channel. Considering (7), Eq.(8) can be simplified resulting independent from V_{ds}. At the initial condition, neglecting the R_{pri} we can consider $V_{ds}=V_{in}$ and thus the (6) is given by

$$\frac{V_{in}}{|V_{th}|} N > 1 \tag{10}$$

3.2.1   Small Signal Analysis

Equation (10) is a good approximation of the more accurate expression of the startup condition that can be derived starting from the equivalent small-signal model of the Classic Armstrong Oscillator shown in Figure III.2, accounting the parasitic of the components.

It is comprised of the small-signal model of the transistor (that include the transconductance, g_m and the drain-source channel resistance R_{ds}), the resistance of the source (R_s), the equivalent DC resistance of the primary and secondary winding of the transformer (R_{pri} and R_{sec}), the gate-source capacitance of the mosfet C_{gs}, the capacitance connecting the secondary winding of the step-up transformer to the gate of the mosfet C_1 and the eventual capacitance loading the oscillator C_L.
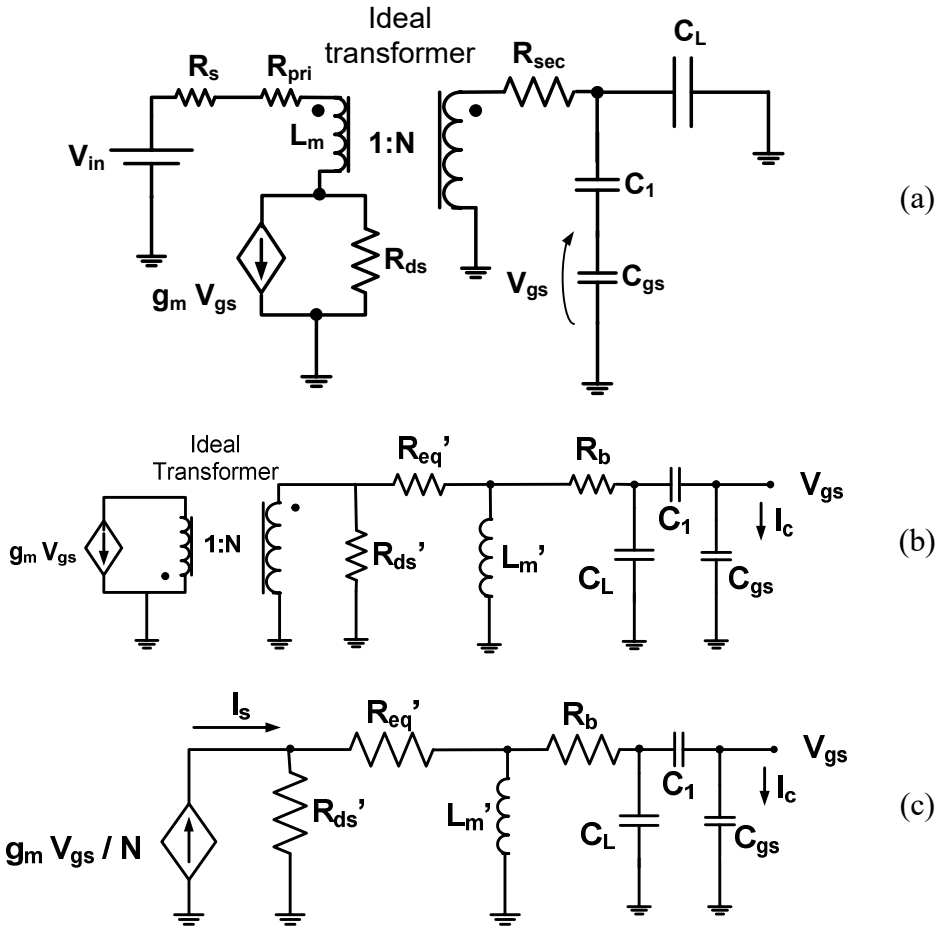
Figure III.2 a) Equivalent small-signal circuit of the oscillator, b) same equivalent circuit of (a) rearranged with all the passive components brought to the secondary side of the transformer; c) same equivalent circuit of (b) rearranged with the active voltage-dependent current-source brought to the secondary side of the transformer.

Figure III.2b and c show the steps needed to rearrange the Figure III.2a to bring all the primary side elements of the transformer (left side) to its secondary side (right side), which means $R_{eq}' = R_{eq}{}^*N^2$ with $R_{eq} = R_s + R_{pri}$, $R_{ds}' = R_{ds}{}^*N^2$ and $R_b = R_{sec}$.

The equivalent circuit at the secondary side of the transformer can be

seen as an equivalent impedance Z_r that transform the current input I_s in the output voltage V_{gs} defined as:

$$Z_r = \frac{V_{gs}}{I_s} = \frac{I_c}{I_s} Z_c \tag{11}$$

Where $Z_c = 1/sC_{GS}$.

Thus the startup condition occurs for the well-known Barkausen criteria conditions.

$$\frac{g_m(V_{gs(0)}, V_{ds(0)})}{N} Z_r > 1 \tag{12}$$

where Z_r can be seen as the passive gain and g_m/N the active gain of the closed-loop gain.

Starting from the right side of the equivalent small-signal circuit in Figure III.2, and recursively applying the current divider between two adjacent paths we can obtain the follow expression:

$$Z_r(S)$$
$$= \frac{S K C L_m R'_{ds}}{(S^2(L'_m + L)C + SCR_b + 1)(R'_{ds} + R'_{eq}) + SL'_m(SCR_b + 1)} \tag{13}$$

Where $C = (C_{gs}\|C_1) + C_L$ and $K = C_1/(C_{gs}C_1 + C_{gs} + C_L + C_L + C_1)$.

Solving the equation for $S = j\omega$ and after some manipulation the self-resonant oscillation frequency can be obtained as:

$$\omega_0^2 = \frac{R'_{ds} + R'_{eq}}{C L'_m(R'_{ds} + R'_{eq} + R_b)} \tag{14}$$

Under the assumption that $R_b \ll R_{ds}' + R_{eq}'$, (14) can thus be simplified

$$\omega_0^2 = \frac{1}{C\,L'_m} \tag{15}$$

The expression of the equivalent impedance is given by

$$Z_r(\omega_0) = \frac{K\,C\,L'_m\,R'_{ds}}{C\,R_b\left(R'_{ds} + R'_{eq}\right) + L'_m} \tag{16}$$

Combining (16) into (12) the startup condition can be satisfied by means of several tradeoff and choosing: a mosfet with high trans-conductance at the initial DC condition but low as possible input capacitance, a transformer with high turn ratio but low as possible DC resistance, R_m (included in R_b).

Importantly, the mosfet switches must have V_{th} as lower as possible in order to work efficiently with low input voltage. In fact the turn on of M_{DEP} occurs when the V_{DS} is approximately:

$$V_{ds} = V_{in} + \frac{[V_{th}]}{N} \tag{17}$$

The larger V_{th}, the larger V_{ds} and the switching power. In order to minimize its power dissipation, the transistor should ideally switch when the applied voltage tends to zero (e.g. Zero Voltage Switching technique).

The depletion mosfet are typically chosen despite the high negative V_{th} introducing an high dissipation during switching between off and on state as show in Figure III.3. This is an important issue for low voltage and power energy harvesting limiting the whole performance of the energy conversion. For this reason and for the (10) the threshold of the mosfet must be, in absolute value, as low as possible.
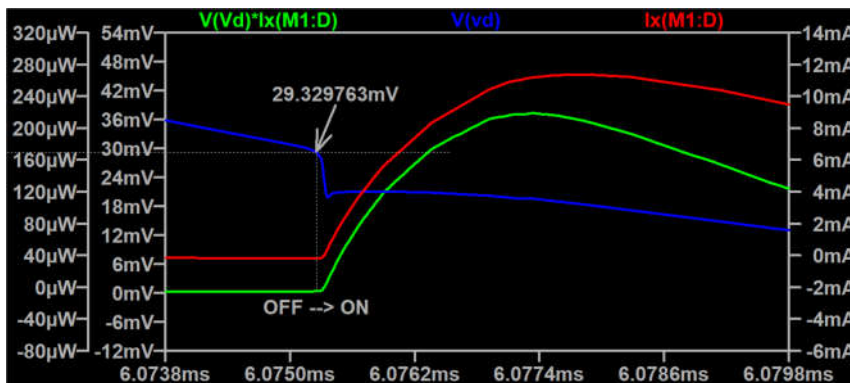
Figure III.3 Typical waveforms obtained simulating in LT-spice the circuit in Figure III.1 using the BSP149 as Mosfet and a $V_{in}=22mV$. V(Vd) represents the drain-source voltage and Ix(M1:D) the current of the mosfet.

To address these issues, the research activity has focused on the possibility to reduce the minimum start-up voltage while maintaining a good efficiency. In order to achieve this result, we propose a variation of the typical Armstrong oscillator topology, which allows the DC-DC converter to operate with an input voltage as low as 11mV.

3.3 Circuit Architecture and Design Guideline

A key requirement for this ultra-low input voltage power converter is to make the circuit internally self-powered. Therefore the goal is to have an ultra-low voltage voltage-booster that requires a minimal amount of startup power at the lowest possible voltage.
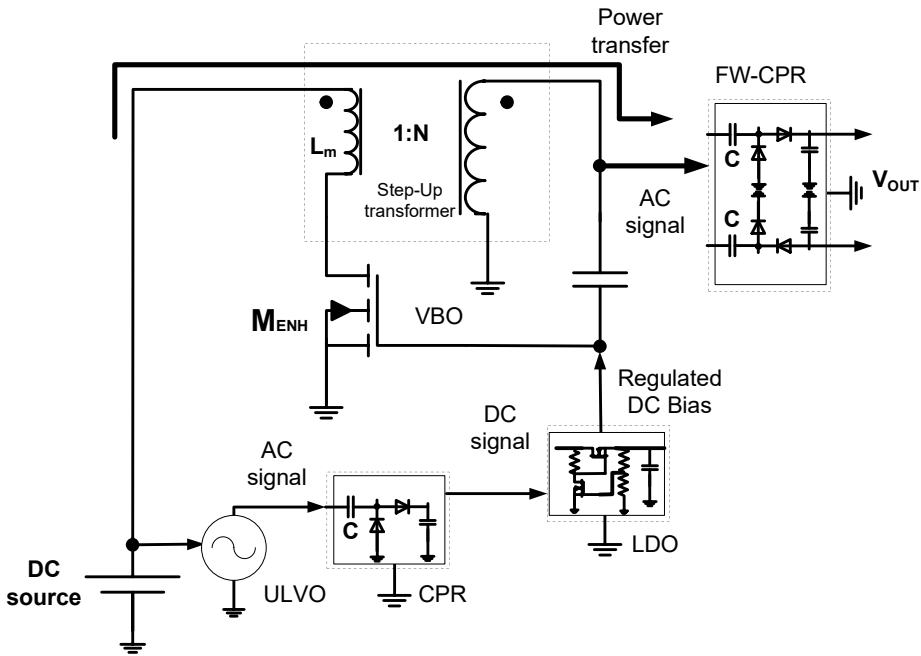
Figure III.4 Block diagram of the proposed DC-DC converter

The circuit architecture realized is sketched in Figure III.4. The basic idea is to bias the gate of the enhancement mosfet (M_{ENH}) with an internally self-powered DC-regulated source. In this way the main limitation of this topologies, i.e. the minimum start-up voltage of 20mV can be overcome as detailed below. The circuit consists of 5 functional blocks:

1. Ultra-Low Voltage Oscillator (ULVO): it is a self-resonant oscillator that converts the low DC-input voltage into a high amplitude AC signal.

2. Charge-Pump and Rectifier (CPR): it doubles and rectifies the AC signal of the ULVO.

3. Low-DropOut regulator (LDO): it regulates the output voltage of the CPR to the optimal value needed for the correct biasing of the VBO.

4. Voltage Biased Oscillator (VBO): it is an Armstrong-oscillator biased and activated by the LDO.

5. Full-Wave Charge Pump and Rectifier (FW-CPR): it comprises two voltage doublers acting on both the positive and the negative waveform of the VB output signal.

With reference to Figure III.4 the operating principle of the proposed DC-DC converter is the following: ULVO is the enabling functional block of the whole DC-DC converter. This block, described in Section3.3.1, converts the low-DC-input-voltage in AC waveform. The output of ULVO is fed into CPR. The CPR boosts and rectifiers the AC-input signal providing a DC output voltage higher than the threshold voltage of the VBO mosfet, M_2.

The LDO-block regulates the output voltage of the CPR to the optimal value needed for the correct biasing of the VBO, which occurs for $V_{gs} \approx V_{th}$. Starting from the initial condition where all the capacitors are completely discharged, the output voltage of the LDO gradually increases and when it reaches the threshold voltage of the M2, the VBO starts to oscillate in switched mode. Since the mosfet trans-conductance reaches

its maximum at the $V_{gs} \approx V_{th}$ the LDO is aimed at dynamically biasing the VBO at V_{th} in order to start the oscillation. Too high values of voltage bias, as results of too high input-voltage, can reduce the efficiency and the average output current capability. This leads to the well-known squegging that blocks or stops the oscillation for a period of time much longer than the period of oscillation. The LDO allows to prevent this issue and extends the input voltage range of the converter avoiding the squegging.

Once the VBO starts to oscillate the high current full-wave charge pump and the rectifier charge the two output capacitors.

In the following I describe in details each building blocks, explaining the circuit operation and showing the design guideline.

3.3.1   Ultra-Low Voltage Oscillator (ULVO)

The enabling function block of the proposed ultra-low voltage DC-DC converter is a new-designed ultra-low voltage oscillator. The oscillator is obtained by modifying the widely used Armstrong topology as show in Figure III.1. The normally-on nMos widely used in literature to enable the self-oscillation is replaced with a zero-threshold nMos, i.e. ALD21290, ensuring both a low start-up voltage and low dissipation during switching. Moreover, an inductor L_2 is added in series to the secondary winding of the transformer in order to improve the start-up condition and oscillation amplitude as described following.

This sub-section is organized as follows. The first part provides an analysis of the proposed ULVO. Finally some preliminary experimental results are shown.

3.3.1.1   Optimized ULVO

The ULVO is obtained by replacing the depletion mosfet with a zero-threshold mosfet, i.e. ALD212900 of the EPAD® MOSFET Family, with increased forward transconductance and output conductance, particularly at very low supply voltages. This allows reducing the power dissipation during switching, the transformer ratio and the associated parasitics.

This zero-threshold voltage mosfet allows the oscillator working with very low input voltage, lower than 6mV. Thus with an input voltage lower than 20mV, the mosfet operates in saturation or, in some cases, near to the saturation or in sub-threshold region. In all cases, the trans-conductance and resistance between drain and source of ALD212900 is sufficient to trigger the oscillation even with very low input voltage. Table III.1 shows a comparison between the parameters of the two mosfets, which is obtained by means of a spice-model simulation under the initial operating conditions.

Parameter	BSP149	ALD212900	Condition
Type	depletion	enhancement	
Vth	(-870mV)	≈0	
gm(S)	1.79E-03	9.30E-06	Vds=6mV, Vgs=0V
ro(Ω)	1.7	1.35E+04	Vds=6mV, Vgs=0V
work region	active	saturation	Vds=6mV, Vgs=0V
gain	0.003043	0.12555	Vds=6mV, Vgs=0V

TABLE III.1 COMPARISON BETWEEN THE TWO MOSFET BY MEANS OF THE SPICE-MODEL PARAMETER EXTRACTION

The gain that we obtain by using theALD212900, is the key aspect to develop an ultra-low voltage boost converter. In fact, thanks to the high gain exhibited by the ALD212900 in condition of zero gate-source

voltage, it is possible to reduce the transformer ratio and consequently the parasitic resistance shown in (16) accordingly to (12).

In addition to the previous considerations an inductor in series with the secondary winding of the transformer is introduced as shown in Figure III.5. The addition of L_2 is beneficial in terms of oscillation amplitude and minimum input voltage requested for the oscillation start-up.
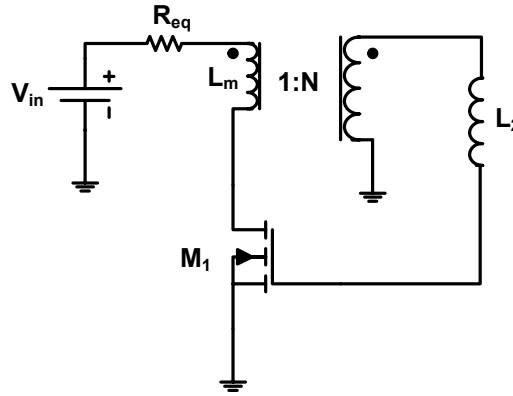
Figure III.5 Proposed Oscillator with an inductor L_2 at the secondary winding of the transformer.

The small-signal circuit of the proposed solution is shown in Figure III.6. With respect the Figure III.2c, now $R_b = R_m + R_2$, where R_2 is the DC parasitic resistance of L_2.
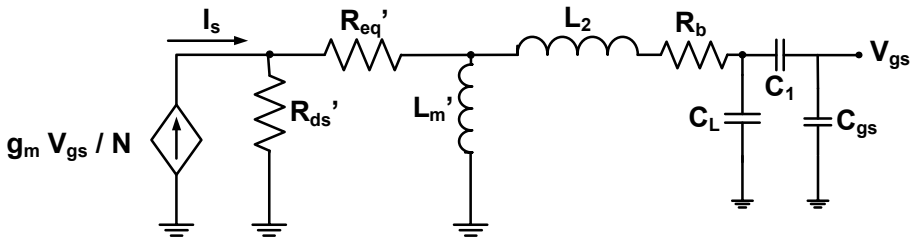
Figure III.6 Small-Signal Circuit

The same procedure discussed in (11) allows calculating the resonance

frequency,

$$\omega_0^2 = \frac{R'_{ds} + R'_{eq}}{C \left[L'_m(R'_{ds} + R'_{eq} + R_b) + L_2(R'_{ds} + R'_{eq}) \right]} \tag{18}$$

Under the assumption that $R_b << R_{ds'} + R_{eq}{}'$, (18) can thus be simplified as

$$\omega_0^2 = \frac{1}{C \, (L'_m + L_2)} \tag{19}$$

Considering (19) the Z_r can be defined as:

$$Z_r(\omega_0) = \frac{K \, C \, L'_m \, R'_{ds}}{C \, R_b\left(R'_{ds} + R'_{eq}\right) + L'_m - \frac{L'_m L_2}{L'_m + L_2}} \tag{20}$$

Comparing (20) to (16), it is evident how the added inductor benefits the startup-condition and the amplitude oscillation. In fact, the key point is to maximize the $Z_r(\omega_o)$, which requires minimizing the denominator of Equation (20). In this perspective, the choice of L_2 is crucial: if L_2 is arbitrarily larger than L_m, (21) simplifies as,

$$L_2 \gg L'_m \; \rightarrow \frac{L'_m L_2}{L'_m + L_2} \approx L'_m \; \rightarrow Z_r(\omega_0) \approx \frac{K \, C \, L'_m \, R'_{ds}}{C \, R_b\left(R'_{ds} + R'_{eq}\right)} \tag{21}$$

However, a larger L_2 implies larger R_2 and R_b, which degrades the start-up of the system. Consequently a tradeoff is needed. The concept is summarized by (22).

$$L_2 \uparrow \; \rightarrow \; R_2 \uparrow \; \rightarrow \; R_b \uparrow \; \rightarrow \; Z_r(\omega_0) \downarrow \tag{22}$$

The optimum results in a transformer 1:16 (Coilcraft , FA2469-AL), L_2 of 12mH and with a DC resistance of 20Ω (22R106C Murata).

In order to further verify the above considerations we compare two

oscillators with and without L_2. The oscillations in both cases are fed into rectifier.

Vin[mV]	without L_2			with L_2		
	Oscillation		Rectified	Oscillation		Rectified
	Pk-Pk[mV]	Freq[kHz]	Vout[mV]	Pk-Pk[mV]	Freq[kHz]	Vout[mV]
5	0	0	0	220	125	34
7	181	166	24	490	125	135
10	366	166	90	750	125	260

TABLE III.2 RESULTS OF COMPARISON BETWEEN TWO OSCILLATORS WITH AND WITHOUT L_2

The results reported in Table III.2 that shows how the introduction of L_2 benefits both the sensitivity and oscillation amplitude. In addition L_2 decreases the oscillation frequency according to (18).

The function of this block is not to transfer a large amount of energy from input to output but to boost the low-voltage DC source to a level suitable for biasing of the VBO. A second normally-on mosfet commonly used in the Armstrong configuration to increase the energy transfer is thus not necessary in this stage, preserving the whole efficiency and start-up sensitivity of the converter.

3.3.2   *Charge-Pump and Rectifier Circuit (CPR)*

The AC voltage produced by the ULVO is boosted and rectified by using a charge pump and voltage rectifier. The charge pump capacitor acts as a load for the ULVO affecting the terms K and C in (20). With reference to Figure III.7, when the voltage across C_{CPR} is close to zero, the load seen by the ULVO is C_L. Thus, C and K of (20) are defined as the parallel between C_{GS} and C_L. C_L is 100nF to ensure the oscillation startup. This block, in combination with the ULVO described in the section 3.3.1,

can boost 10mV-DC input over the threshold voltage (typically 1V) of M_2 guaranteeing the correct operation of the VBO.
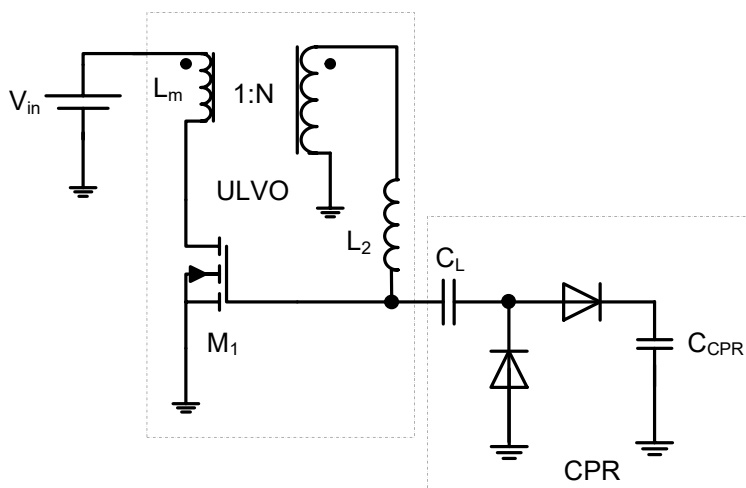
Figure III.7 ULVO and CPR circuit

3.3.3   *LDO*

The LDO compensates the unpredictable variations of the available power at the source, keeping constant the output voltage, V_{LDO} at the optimal value required for the VBO biasing. The transistor level implementation of the proposed voltage regulator is depicted in Figure III.8. LDO block has two important functions:

- The regulation of the output voltage of the CPR to the optimal value needed for the correct biasing of the BS.
- To avoid the Squegging phenomenon that can occur when a charge builds up on the coupling capacitor C_4, which shifts the DC bias point suppressing the oscillation for a certain period of time.

This block has to be designed in order to obtain a power consumption as lower as possible at low input-voltage. This is very important to avoid overloaded ULVO. In this perspective ALD21290x device are the key components due to the tight threshold voltages control, which enables predictable transistor operation at very low voltages and current.
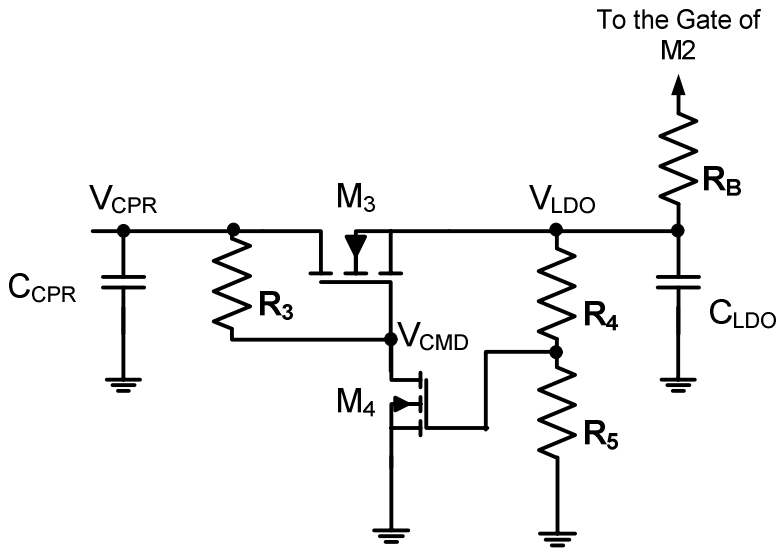
Figure III.8 LDO circuit

In the LDO circuit, shown in Figure III.8, M_3 has the function of pass-transistor between the input and the output, respectively V_{CPR} and V_{LDO}. The gate of M_3, V_{CMD}, is driven by R_3 and M_4 that act as an inverter supplied by the input voltage, V_{CPR}. M_4 is controlled by means of two feedback resistors, R_4 and R_5. The V_{CPR} rise increases V_{CMD} and consequently the source-gate voltage of M_3, as well as V_{LDO}. A higher V_{LDO} forces an increase of V_{CTRL}, counteracting the initial V_{CMD} variation. Therefore, the LDO behaves as an active DC regulator, clamping the DC output voltage, V_{LDO}, at the optimal value for the VBO biasing (achieved

through R_B). $R_3 = 10M\Omega$, $R_4 = 10M\Omega$ $R_5 = 8M\Omega$ and $R_B = 100k\Omega$ have been chosen, after simulations and empirical tests, in order to minimize the load applied to the ULVO yet without compromising its regulation.

3.3.4   *Voltage Biased Oscillator (VBO)*

The second oscillator has been designed to maximize the energy conversion and transfer between the source (V_{in}) and the output (V_{o+}, V_{o-}). We used an enhancement M_2 (IRLML6346TRPbF) that exhibits a threshold voltage of about 800mV and high current capability.

The nominal parameter values (g_m and r_{ds}) reported in the datasheet and confirmed through spice-simulations are summarized in the Table III.3 at different work conditions (V_{gs} and V_{ds}).

Parameter		Condition		Calculation	
g_m[mS]	$r_o[\Omega]$	V_{gs}[V]	V_{ds} [mV]	N	(6)
23.4	7.6	0.8	10	20	3.5568
76.9	0.9	1	10	20	1.3842
104	0.284	1.25	10	20	0.59072
23.4	7.6	0.8	10	50	8.892
76.9	0.9	1	10	50	3.4605
104	0.284	1.25	10	50	1.4768

TABLE III.3 IRLML6346TRPBF MOSFET PARAMETER AND SIMPLE CALCULATION OF (6) FOR THE VBO

Looking at the Table III.3 and biasing the gate of the transistor slightly above its threshold voltage (about 800mV) with the two blocks described in the sections 3.3.1, 3.3.2 and 3.3.3 the mosfet will work near to the saturation region ensuring the condition in (6) also with a transformer ratio 1:20. In order to improve the oscillation startup and to increase the

oscillation amplitude we have used for this oscillator a transformer with a winding ratio of 50 (Wurth 774 8854 0120) as depicted in Figure III.9.
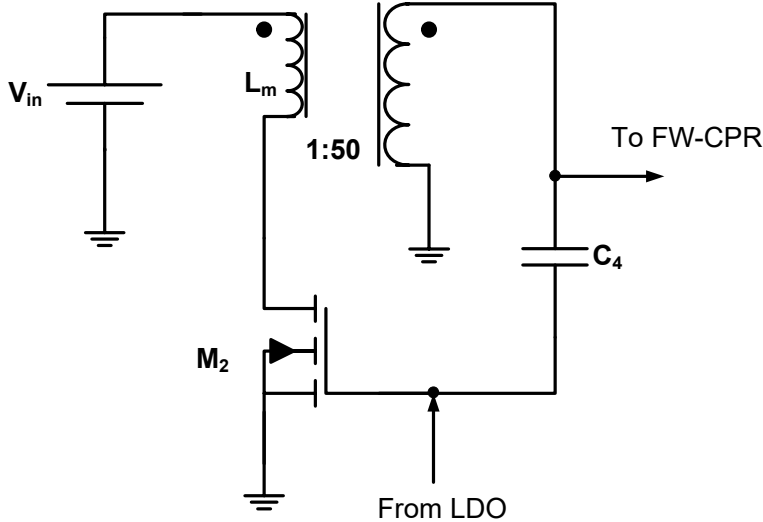
Figure III.9 BSO circuit

3.3.5   *Full-Wave Charge Pump and Rectifier*

The AC voltage waveform generated by the VBO, is boosted and rectified by a full-wave charge pump voltage doubler which duplicates the voltage acting on both the positive and negative voltages. The circuit shown in Figure III.10 represents a pair of voltage doublers of opposite polarities. The output of the circuits is taken between the terminals of the two voltage doublers. A capacitor, C_{out+}, is charged up to the AC voltage peak on the positive half cycle while the other, C_{out-}, is charged up during the negative half cycle. Since the target load is connected between these two capacitors, it is subject to a voltage difference that is fourth times the amplitude, V_{osc}. Since C_{out+} and C_{out-} are both part of the total reservoir capacitance and each one is charged on alternative half cycles, the total

reservoir receives a charging pulse twice every mains cycle, so it is a full wave circuit. The output voltage, V_{OUT}, is defined as the difference between the voltage across the two capacitor, V_{o+} and V_{o-}:

$$V_{OUT} = V_{o+} - V_{o-} \tag{23}$$
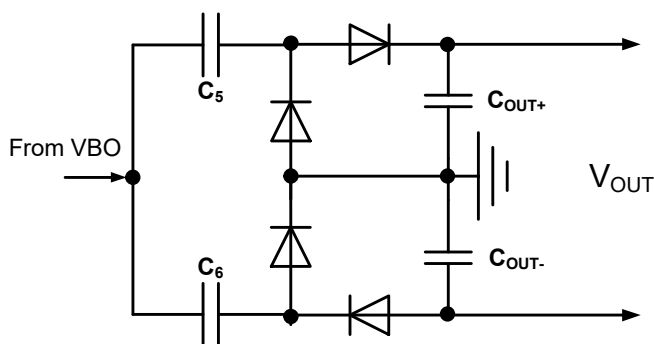
Figure III.10 FW-CPR circuit

3.4 Measurements and Results

The measurements performed on the whole circuit shown in Figure III.4 are discussed in this section.

We tested the DC-DC converter electrical performances using the DC Power Analyzer, N6705B, and the Agilent DSO3034A oscilloscope. The tests was conducted by measuring the performance of the DC-DC converter in terms of:

- The Minimum input-voltage V_{in} necessary to charge the two completely discharged output capacitors to a suitable voltage level of at least 1.8V(to power for example microprocessors, or wireless sensor nodes).

- The Charge Time (T_c) and the Charge Efficiency (η_C) for different V_{in}

- The DC-DC Input Resistance (R_{in}) to match the output impedance of the voltage sources (i.e. TEGs).

All the measurements we performed by considering the same two output capacitors, 1mF for each charge-pump rectifiers as described in section 3.3.5. Thus, the equivalent capacitor at the output was 500uF in all the measurements.

We characterized also the performance of the DC-DC converter connected to a TEG (Laird HT2,12,F2,3030).

In conclusion, a duty-cycled wireless application taking into account the power consumption of the CC2650 of the Texas Instruments, is proposed.

Figure III.11a shows the typical Input Current (I_{IN})-Time and Output Voltage (V_{OUT})-Time curves measured for V_{IN}=14.6mV. The I_{IN} and the two output capacitor voltages (V_{o+} and V_{o-}) have been acquired on three different channels of the N6705B. Figure III.11b shows the initial portion of the larger acquisition depicted in Figure III.11a. V_{OUT} starts to increase after a few seconds. This is the time needed by the ULVO to start-up and to bias VBO mosfet at its threshold voltage. Once the VBO transistor is correctly biased the DC-DC starts transferring energy from the input to the output, charging the two capacitors. When V_{OUT} increases the I_{IN} slowly decreases and then also the output current decreases.

(a)   (b)
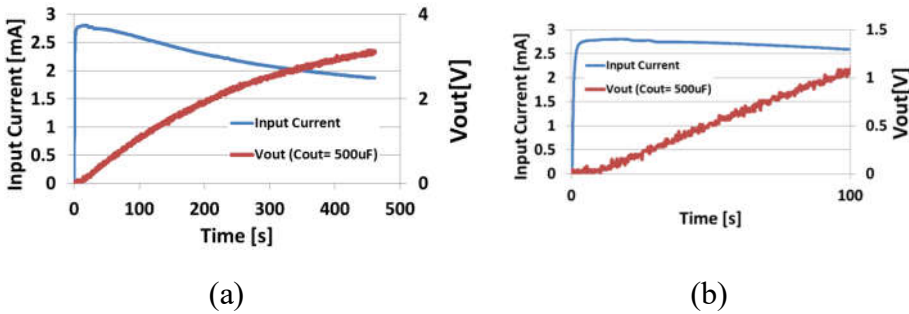
Figure III.11 a) Input Current and Output Voltage over Time for Vin=14.6mV; b) detailed view of the first 100s of the acquisition.

Figure III.12 shows the charge time T_c vs V_{IN} at two different V_{OUT} (2.1V and 3V) both suitable to power microprocessors, or wireless sensor nodes. For a $V_{IN} \sim 11$mV the time needed to charge the two completely discharged capacitors to 2.1V is 524s. Around 12mV-input voltage the converter needs only 260s. At this minimum input-voltage, the DC-DC converter can charge the capacitor over 3V in 530s. The efficiency η_C, calculated as the ratio between the output and input power at $V_{OUT} = 3$V, is shown in Figure III.12b. The peak of efficiency, about 34%, occurs at

V_{IN}=13mV and is better than the efficiency obtained by [13] also with higher input voltage (20mV), confirming the goodness of the proposed solution. In fact the circuit has been optimized to work at low input voltage.

<div align="center">(a)   (b)</div>
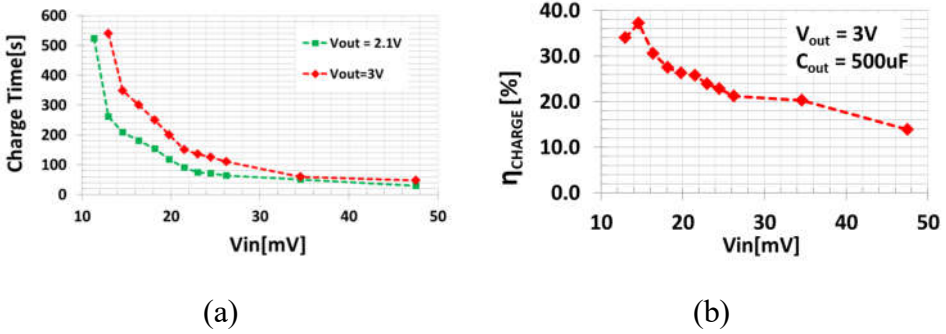
Figure III.12 a) charge time T_c vs input voltage V_{in} , for two different V_{out} ; b) charge efficiency (η_C) vs V_{in}

In order to collect the maximum amount of power available from a given source the converter impedance must match the source

<div align="center">(a)   (b)</div>
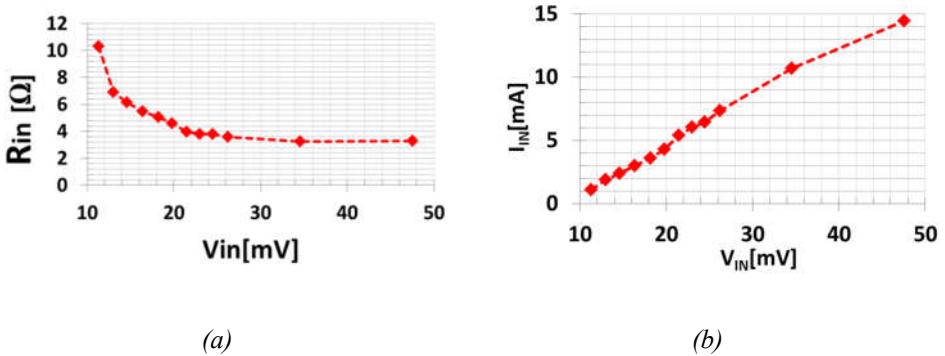
Figure III.13 a) Input resistance of the proposed DC-DC converter vs Vin; b) Input current absorbed by the DC-DC converter vs the input voltage.

The proposed circuit exhibits a low input resistance as shown in Figure III.13a, ensures a nearly optimal power transfer with different sources,

(such as TEGs) and draws current from the low-voltage source as depicted in Figure III.13b.

Commercial TEGs offer an internal resistance that varies from 0.8 to 6Ω [43]. The low input resistance offered by the proposed DC-DC converter ensures a nearly optimal power transfer with different TEGs.

The size of the TEG required for a given application depends on the minimum ΔT available, the maximum power required by the load, as well as the thermal resistance, R_{Th} of the cold side. R_{Th} is the most critical parameter for power generation purpose. By increasing the R_{Th} from 1°C/W to 10°C/W the output power generation decreases by 95%. The use of a heat sink (cold side) with the lowest possible thermal resistance R_{Th} maximizes the electrical output by maximizing the temperature drop across the TEG (ΔT).
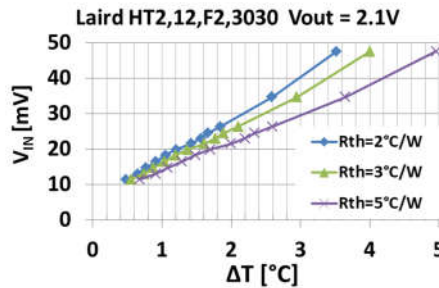
Figure III.14 input voltage V_{in} vs thermal gradient ΔT applied between hot and cold junctions of the TEG.

Figure III.14 shows the voltage measured at the DC-DC converter terminals (V_{IN}) when it is powered by the TEG under different ΔT conditions. In order to achieve the specific R_{Th} conditions different heat sinks of the WAKEFIELD Thermal Solution were used. The

measurements, as depicted in Figure III.14, were realized starting from $R_{Th}=2°C/W$ as it is technically difficult to obtain a lower value.

In Figure III.15a an example of duty-cycled wireless sensor application powered by the TEG is simulated. The relation V_{in}-ΔT is the same of the Figure III.14. The results are achieved considering the BLE power consumption of the CC2650 Wireless MCU (Texas Instruments). The CC2650 with a very low active RF and low-power MCU provides excellent battery lifetime and allows for operation on small coin cell batteries, also it is suitable for energy-harvesting applications. The parameters used for the power consumption simulation were the results of the BLE tests carried out on CC2650 device running a demo application with 100 data packets sends per second for different level of power transmission and voltage power supply as reported in the Table III.4.

I_{PULSE} [mA]		V_{DD} [V]			
t_{PULSE}[ms] 3.1		2.1	2.7	3	3.3
P_{TX} [dBm]	5	5.62	4.24	3.97	3.72
	0	5.37	3.88	3.68	3.59
	-6	5.13	3.74	3.56	3.48
	-15	4.99	3.76	3.41	3.36
	-21	4.78	3.68	3.45	3.27

Table III.4 CC2650 CURRENT CONSUMPTION DURING BLE TRANSMISSION

To support pulsed application, a reservoir capacitor has been dimensioned to ensure the total pulsed-current for the transmission and to obtain the lowest voltage drop. As reported in [43] the capacitor is dimensioned according to the following formula.

$$C_{OUT} > \frac{I_{PULSE} t_{PULSE}}{\Delta V} \qquad\qquad (24)$$

Where $\Delta V = 40mV$ is the allowed drop-down voltage on the reservoir capacitor C_{out}, $I_{pulse} = 6mA$ is the average current during the transmission, $t_{pulse} = 3mS$ is the duration of the transmission. Given these requirements C_{out} must be 470uF. The equivalent C_{out} of 500uF, used in the previous measurements, is sufficient. Considering that the stand-by current between transmit pulses can be very small, (about 2.7uA), the outputted current is able to recharge the capacitor during the interval between load pulses as depicted in Figure III.15b.

(a)   (b)
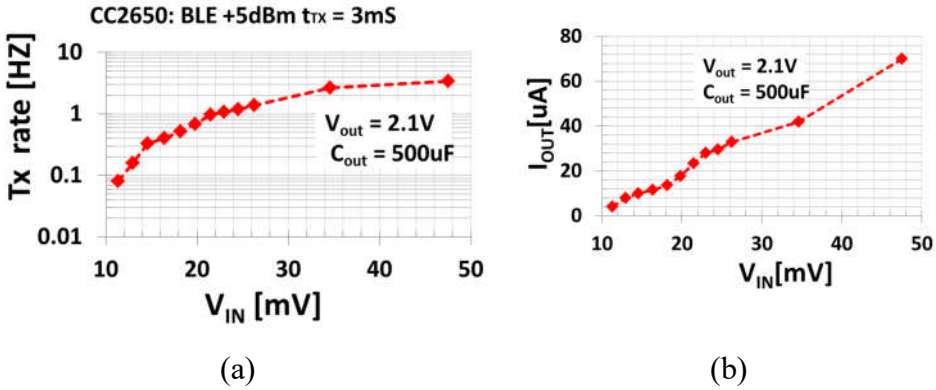
Figure III.15a) Example of duty-cycled application simulation with different V_{in}; b) the outputted currents from DC-DC converter in function of the V_{in} at $V_{OUT}=2.1V$.

A simple way to estimate the maximum duty-cycle is to divide the net current charging the capacitor during the stand-by mode of the CC2650 by the average current during the transmission. The maximum transmit burst rate that the harvester can support is defined as the ratio between the duty-cycle and the t_{pulse} and depends on the input voltage as shown in Figure III.15a.

3.5 Conclusions

A new ultra-low-voltage DC-DC converter able to boost 11mV-input voltage to 2.1V output voltage has been presented. The converter can charge a completely discharged 500uF capacitor above 2.1V in 524s starting from 11mV. The proposed solution reduces the conversion threshold of the traditional and commercial DC-DC converter by a factor two.

The proposed DC-DC circuit has been optimized to convert power from low voltage source, such as TEGs. In fact the internal resistance of the commercial TEGs can be well-matched with the proposed DC-DC converter. The converter tested with an input thermal range between 0.6 to 4°C, can support low-power pulsed-load application, such as a low duty cycled BLE transmission with a transmit burst rate over the range of 0.08 - 3.4Hz.

Chapter IV
Sensors

During the past four decades, the term "sensor" evolved from the concept of mere passive probes (e.g., thermistor used as temperature sensor) towards the concept of active smart devices able to measure and locally process information. Sensors have become widespread in every industrial automated production and logistic environment and consumer applications. With advance in easy-to-use microcontroller platforms, the use of sensors expands beyond the traditional application fields, such as temperature, proximity and flow measurement.

In this scenario, the quest to achieve ever-lower power consumption levels and lower cost for the smart-sensor has become a must that has placed difficult challenges on engineers. In the following section we discuss about innovative low-cost and low power sensor exploiting heterogeneous technologies.

This chapter is organized as follow.

Firstly, a self-powered and ultra-low cost triboelectric flowmeter suitable for flow metering of gases or fluids is presented. Differently from other flowmeters presented in the literature, the prototype we realized is based on the triboelectric effect allowing obtaining a self-powered transducer. The realized device is extremely low cost because it uses commercial silicone as triboelectric material. The comparison between experimental measurements and output data of a commercial flowmeter,

used as reference, demonstrates the effectiveness of the proposed solution in both constant and variable flow conditions. The proposed solution can be used also as a starting point in the development of a fully self-powered smart flowmeter exploiting their energy harvesting capabilities.

Secondly,the first ultra-low voltage and power displacement sensor based on eddy current principle is presented. The aim of the research work is to demonstrate the possibility to have at least 10μm-displacement resolution with a power consumption lower than 100uW. The designed optimized circuit is able to detect a 6μm-displacement with an input voltage of 100mV and a power consumption of 28uW.

4.1 Self-Powered and Ultra-Low cost Triboelectric Sensor for Smart Flow Metering

In the last few years, thanks to the advances in emerging and enabling technologies like wireless connectivity and energy harvesting system, the smart metering received a growing interest resulting in a boost of research activities in both industry and academic domains. In this scenario, new flowmeters for civil and industrial applications gained renewed attention as demonstrated by the number of papers presented in the literature. Most of the presented solutions refer to enhanced versions of devices based on well-known transduction principles.

For example, electromagnetic flowmeters (e.g. [46]), are obstruction-free systems and have their main advantage in the not interruption of the flow in the pipe, but they do not work with non-conductive fluids. Coriolis mass flowmeters do not suffer from this limitation and keep the non-invasive feature, but are based on the mechanical oscillation of the pipe and it is essential to have a closed-loop control system to keep stable the oscillation and consequently obtain higher precision and stability of the measurement, (e.g. [47]). Vortex flowmeters, instead, are suitable for measuring all types of fluids or gases, but are not obstruction-free. In real applications the measurement is affected by impacts and vibrations occurring during the normal operation, and therefore require complex signal processing algorithms to eliminate these effects on the measurement, (e.g. [48]).

Optical and ultrasonic flowmeters have the advantage of non-contact measurement with the fluid or gas flowing through the pipe, therefore are

very useful for applications with extreme temperatures or highly polluted fluids, and gases. They can use several mechanisms like Doppler effect, laser beams (e.g. [49]), or sound pattern (e.g. [50], [51]) and are based on the cross-correlation of known signals disturbed by the fluid flowing through the pipe. Their main disadvantages are the strong dependence on the acoustic properties of the fluid that can be influenced by environmental factors (e.g. temperature), the material properties of the fluid (e.g. low density, especially in case of gases),the impurities in the fluid itself and the very small amplitude of the signals that have to be processed.

The solution proposed in this chapter aims to overcome the main drawbacks of classic flowmeters by using triboelectricity as transduction mechanism. Differently from the classic flowmeters, there is no need to power supply the transducer allowing obtaining a self-powered device. Indeed, thanks to the transducer architecture described in the following, it is possible to estimate the amount of material flowing through the device (air in our case) by measuring the frequency of the voltage pulses generated by the realized device. Indeed, like in classic Hall effect-based mechanical flowmeters, the frequency of the voltage pulses is directly proportional to the velocity of the fluid flowing through the device. By knowing the section of the pipes, it is possible to obtain the desired flow measurement.

Moreover, the proposed device has been designed with a very simple and effective architecture that is enabling for redundant measurements and triboelectric energy harvesting capabilities that in turn help in the implementation of a fully self-powered smart sensor.

The section is organized as follows. In Section 4.1.1 we describe the realized prototype, while its operating principle is detailed in Section 4.1.2. The measurement setup and the experimental results are presented in Section 4.1.3. Section 4.1.4 concludes the chapter.

4.1.1   System Description

The exploded sketch of the TriboElectric Flowmeter (TEF) we realized is shown in Figure IV.1. All the mechanical parts have been realized in ABS (Acrylonitrile Butadiene Styrene) using a commercial 3D printer. To validate the proposed solution we used the air flow provided by a portable air compressor. The system is comprised of two main parts. The first one (i.e. Main Body) resembles the classic structure of impeller-based flowmeters, while the second one (i.e. Crankcase) includes the triboelectric transducer.

When a gas/fluid flows through the main body induces the rotation of the impeller into the main body, which in turn activates the rotation of the triboelectric impeller into the crankcase thanks to the rigid connection realized by the shaft.

The crankcase is a dry chamber isolated from the main body by means of gaskets. Consequently, the measurement is independent of the gas/fluid flowing into the main body and it is related only to the rotation speed of the triboelectric impeller and to the internal diameter of the incoming and out coming pipes of the main body.

The four-blade impeller inside the dry chamber operates as a triboelectric element. A 0.2 mm thick layer of commercial acetylic silicone has been deposited onto the surface of the impeller facing to the

closure cap. In the triboelectric series, the silicone is one of the most electronegative materials (i.e. with a great tendency to gain electrons) while the ABS used to realize the impeller is neutral from a triboelectric effect point of view. The silicone in gel form has been deposited at room temperature and let solidify. The crankcase closure cap, instead, is realized using a double-sided 1.6 mm thick FR4 board with 35 μm of copper on each side. The surface of the closure cap faced to the impeller has been divided into eight sectors by mechanical milling, and an electric contact for each sector has been realized. Each sector has the same physical dimensions (and same area) of a blade of the triboelectric impeller.

From an electric point of view, two adjacent sectors (namely S- and S+) form a pair of positive and negative contact from which is possible to measure the output voltage generated by the rotation of the triboelectric impeller. Consequently, the whole cap has been divided into four pairs of sensing elements (i.e. sectors S_i, where i = 1,2,3,4). By combining opportunely the electric contacts of the four sectors, it is possible to obtain different configurations of the device. For example, with four independent pairs of sectors, it is possible to obtain a redundant measurement. Alternatively, it is possible to use just one sector for flow metering while the remaining three sectors can be connected in parallel in order to obtain an equivalent larger active area of the triboelectric device that is fine for energy harvesting purposes.

In this work, we focused on the validation of the measuring capabilities of the proposed flowmeter, neglecting its energy harvesting capability.
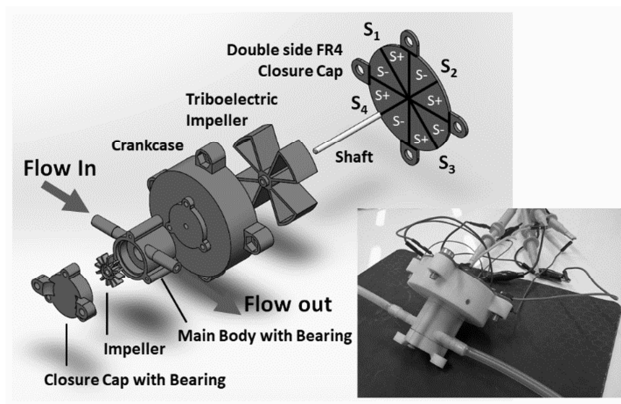
*Figure IV.1 Exploded 3D sketch of the proposed TEF prototype. The fully assembled
prototype is shown in the inset.*

4.1.2   *Operating Principle*

The silicone surface of the impeller and the copper surface of the
closure cap have been put in contact and separated during the assembly of
the whole device. In this way, a negative charge has been induced into the
silicone layer of the impeller because of the tribo-electrification process
(i.e. transfer of electrons from the copper surface of the closure cap to the
silicone).

Once fully assembled, the realized transducer resembles the structure
of a single dielectric triboelectric device operating in non-contact mode,
as schematically depicted by the 4-step sequence shown in Figure IV.2.
For sake of simplicity, the following description refers just to a pair of
adjacent sectors (i.e. only one S+ and one S-) and one blade of the
triboelectric impeller.

The basic assumption is that the initial amount of triboelectric charge,
Q, obtained by putting in contact the triboelectric blade and the closure

cap during the assembly of the device remains constant during the rotation of the impeller because the device operates in non-contact mode. In this way, by changing the capacitive coupling between S- and S+, represented by the parameter C, it is possible to obtain a voltage generation, V, across the S- and S+ terminals because of $Q=C \cdot V$. The variation of C can be easily obtained by exploiting the rotation of the triboelectric impeller that causes a variation in the overlapping between the impeller itself and S+ and S-.
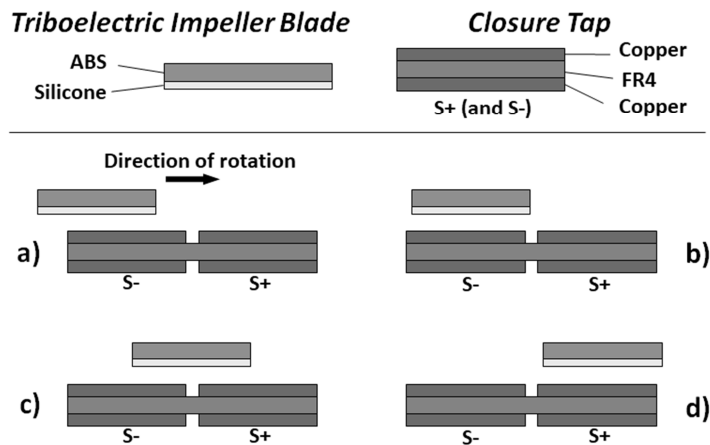
Figure IV.2 Four-steps sequence of the operating principle of the proposed TEF a) approach; b) cross; c) overlap; d) overtake. The material stacks used for the triboelectric impeller blade and the closure cap (with the copper electric contacts) are sketched in the upper side.

The experimental output voltage generated by the TEF shown in Figure IV.3 confirms this behavior. As it is possible to note while the impeller blade is far from the gap between S- and S+ (see Figure IV.2a), or it overlaps the gap (see Figure IV.2c), there is no change in C and consequently no ΔV is generated between S- and S+.

Vice versa, when the blade crosses and overtakes the gap between S-

and S+ (Figure IV.2b and Figure IV.2d, respectively) a ΔC occurs, and consequently a negative voltage pulse, and a positive one are generated, respectively. The frequency of the pulse train generated by the cyclic sequence of the four phases described above is related to the rotation speed of the triboelectric impeller, and consequently to the speed of the gas/fluid flowing through the main body of the TEF.

The gap between the closure cap and the triboelectric impeller in the dry chamber strongly influences the proper operation of the device. In non-contact triboelectric devices, indeed, the closer is the gap the higher is the sensitivity of the triboelectric transducer, [52]. In the prototype we realized, the gap is about 2.0 mm, due to mechanical constraints of the realized crankcase.

The initial charge generated by the triboelectrification process can not be stored by the silicone layer of the triboelectric impeller indefinitely. It has a decay time that depends strongly on the environmental conditions (e.g. humidity) and on the properties of the material used, [53]. In any case, in further TEF implementations, it can be regenerated by periodically put back in contact the triboelectric impeller and the copper closure cap.
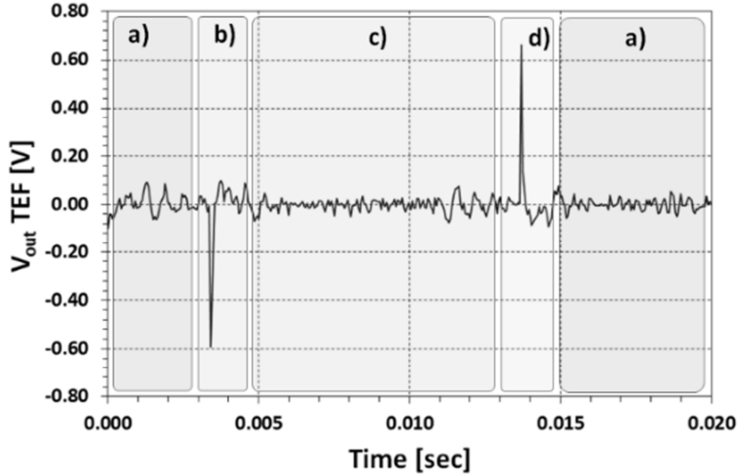
Figure IV.3 Output voltage generated by the TEF in conditions of low air flow to highlight the corresponding steps of the sequence shown in Figure IV.2.

4.1.3   Experimental Results

The realized prototype has been characterized by using the setup shown in Figure IV.4. The air exits from the blow gun of the portable air compressor and is canalized into the realized TEF by a flexible rubber pipe. The air exiting from the TEF flows into a second flexible rubber pipe and enters in the commercial Hall Effect-based flowmeterused as reference transducer. In this way, the two flowmeters are connected in series and are subjected to the same air flow. Both the output voltage generated by the TEF and the output signal of the Reference Flowmeter (RF) are acquired with an Agilent DSO9254Aoscilloscope.The RF is powered by an Agilent E3631A power supply.

It is important to note that the main body of the TEF, resembling the structure of a classic impeller-based flowmeter (see Figure IV.1), has been designed reproducing the same mechanical dimensions of the

commercial flowmeter (i.e. same internal diameter of the pipes, same
dimensions and same number of blades of the impeller). Moreover, the
triboelectric impeller has been designed with four blades in order to have
four output voltage pulses per round, the same ones of the RF.
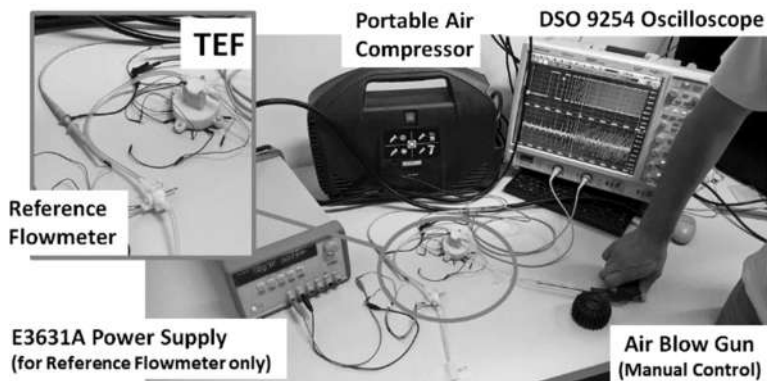
*Figure IV.4 Experimental setup. The inset shows a zoom of the realized TEF and the
reference flowmeter connected in series*

In this way, it has been possible to compare directly the pulse sequence
generated by the TEF with the one generated by the RF, validating the
proposed solution.

Figure IV.5 shows an example of comparison between the two output
signals provided by the RF and by the proposed TEF when operating with
a constant (on the left) and a variable (on the right) air flow once
synchronized in post-processing. As it is possible to note, there is a very
good agreement between the voltage peak (negative or positive) generated
by the TEF and the rising and falling edges of the RF output signal.
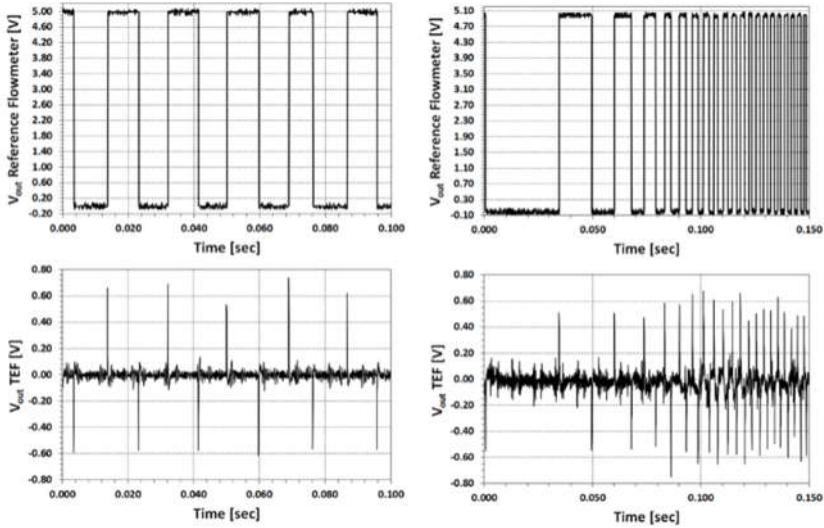
*Figure IV.5 Comparison between the output signal of the reference flowmeter and the
output voltage generated by the TEF measured across the S- and S+ terminals of the
sector S1 in case of constant (left) and variable (right) air flow*

The slight differences in the peak amplitude of the TEF output signal
are related to two different aspects of the TEF prototype fabrication
process. The first one is the non-uniform thickness of the silicone layer
due to the manual deposition process. The second one is the slightly
eccentric rotation of the triboelectric impeller due to the mechanical
tolerance of some 3D-printed parts. Both these aspects produce the same
macroscopic behavior: a variation in the gap between the triboelectric
impeller and the closure cap during the normal operation of the TEF.As in
any triboelectric/electrostatic device, indeed, a variation of gaps or
overlaps between its elements produces a variation of its equivalent
capacitance, with a consequent variation in the voltage generation. It is
worth noting that these non-idealities do not affect the flow rate
measurement because it is based on the frequency of the pulses and not on

their amplitude.

The amount of air flowing into the TEF can be estimated by knowing the mechanical parameters of the main body of the TEF (i.e. internal pipe diameter), measuring the time interval between four consecutive peaks of the same sector (either positives or negatives) and implementing a classic Frequency-to-Voltage converter.
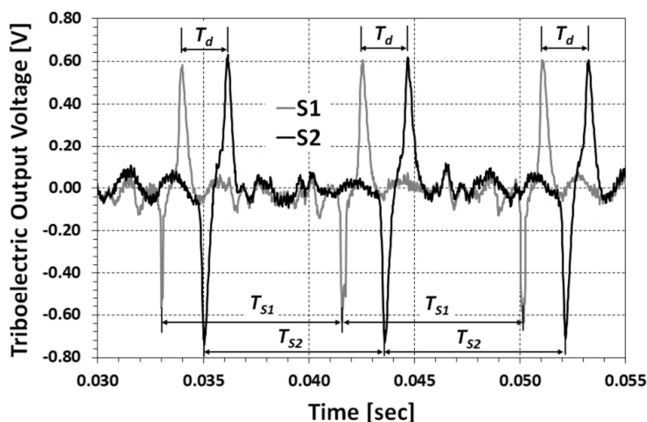
Figure IV.6 Output voltage signals generated by the two adjacent sensing elements S1 and S2 of the realized TEF, in case of constant air flow

Figure IV.6, instead, shows an example of measurements of the output voltage generated by two adjacent sectors of the TEF (i.e. S1 and S2) in case of constant air flow. As expected, they present the very same behavior and, accordingly with the rotation direction, the pulses occur in the very same order (i.e. first S1 followed by S2). Moreover, the delay, T_d, between the pulse generated by S1 and the corresponding one generated by S2 is constant because of the air flow is constant (i.e. the triboelectric impeller rotate at constant speed).

From a practical point of view, it is easy to determine the rotation

direction of the impeller and consequently the direction of the air flow by the simple analysis of the sequence in which the pulses occur (e.g. S1-S2-S1-S2-… means clockwise rotation direction of the impeller, S2-S1-S2-S1-… means counterclockwise rotation direction). At the same time, it is possible to obtain a redundant measurement, by comparing the time interval between two consecutive positive (negative) pulses of S1, T_{S1}, and the corresponding T_{S2} of S2.

4.1.4 Conclusion

In this chapter, we presented a self-powered ultra-low cost triboelectric transducer suitable for flow metering of gases or fluids. The transducer exploits commercial silicone as triboelectric material.

The effectiveness of the proposed solution is demonstrated by the very good agreement resulting from the comparison between the output data of the realized prototype and the ones provided by the commercial reference flowmeter.

Finally, thanks to the possibility of the realized prototype to reconfigure the electric contacts, it is possible to enable additional features like flow direction detection or even energy harvesting capabilities, that is useful in order to design a fully self-powered smart flowmeter.

4.2 Ultra-Low Voltage and Power Displacement Sensor

The demand of displacement sensors is rapidly increasing with the proliferation of industrial automation. At the same time, we observe a strong request to achieve ever-lower power consumption technologies and low cost displacement sensors. Displacement sensors have an important role in the sensor world because of their intrinsic capabilities to estimate multiple quantities such as pressure, acceleration, etc., which make their application range very wide.

These sensors typically exploit optical, capacitive, and eddy current principles. Optical sensors usually have high resolution with large measurement range, but they are often expensive, sensitive to optical contaminations and power hungry. Capacitive sensors can achieve extremely high resolution, but target grounding is necessary and they are sensitive to the properties of dielectrics placed in the measuring gap[54].

Conversely, Eddy Current Sensors (ECSs), operating on the principle of magnetic induction, can precisely measure the position (Displacement, x) of a metallic target in contaminated environments (e.g. dust, oil particles, etc.) and also through non-metallic materials such as plastics, dirt, etc.[55]. The main drawbacks of ECSs is the high thermal drift that under uncontrolled conditions can negatively impact the measurement precision.

ECSs are widely used in industrial applications for direct displacement measurements or indirect quantities measurements (vibration, acceleration, etc.), also they can be used to estimate material property, detect crack fatigue inspection.

Different methods have been developed to enhance the resolution and reduce the thermal drift, such as measuring the working frequency, precise amplitude demodulation, etc. However, none of these methods can ensure ultra-low power performance. In fact, many works [55] to [57] show that the power consumption cannot be lower than 5mW.

This Section presents a simple design and implementation of an ultra-low-power and voltage micrometric-resolution-eddy current displacement sensor. The purpose of this work is to demonstrate that a 10μm-resolution eddy current sensor can achieve a power consumption lower than 30uW even supplied with a voltage constant room temperature in order to eliminate any thermal drift issue.

This Section is organized as follows. In Section 4.2.1 we describe the operating principle of the sensor, which is subsequently modeled in Section 4.2.2. Section 4.2.3 describes more in detail the proposed low-voltage and low-power eddy current displcement sensor. The experimental results are presented in Section 4.2.4. Section 4.2.5 concludes the sub-chapter providing the results summary.

4.2.1   Operating Principle

A typical ECS system consists basically of a sensing coil, and a conductive target. As shown in Figure IV.7a, the coil is excited by an ad-hoc signal generated by a control unit.
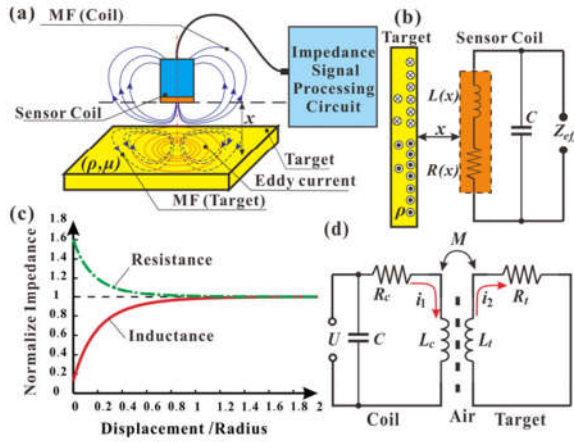
Figure IV.7a) Typical ECS schematic; b) Equivalent circuit of an ECS; c) Typical inductance and resistance responses over x; d) Transformer model of ECS. Re-plotted from[57].

The sensor coil, driven by an AC current, generates alternating magnetic field, which concatenates with the nearby conductive target inducing eddy currents. In turns, eddy currents generate magnetic field, which is opposite to the one generated by the coil. This causes a magnetic flux reduction and energy dissipation in the coil. With reference to Figure IV.7c, the proximity of the conductive target influences both the coil inductance L_c, and the series resistance, R_c. More precisely, by moving the target closer to the inductance L_c increases, whereas the resistance R_c decreases. At the coil terminals, this results in a variation of the equivalent sensor impedance, Z_{eff}, depicted in Figure IV.7b. The impedance Z_{eff} can be represented as the parallel between Z_x, formed by the R_x-L_x series, and a capacitance C forming a LC tank. The capacitance C includes also the parasitic capacitance of the coil.

The relationship between Z_x and the target position x depends on the characteristics of the sensor coil, on the working frequency, and on the

properties of the target. All this can be summarized with reference to [57], with the following equation

$$Z_x = R_x + j\omega L_x$$
$$= [R_c + R_e(x, \sigma, x, \mu)] + j\omega[L_c - L_e(x, \sigma, x, \mu)]$$

(25)

where R_c and L_c are the resistance and inductance of the sensor coil; R_e and L_e are the resistance and inductance caused by the eddy current; σ is the electronic conductivity of the target; μ is the permeability of the target; f is the working frequency of the ECS. The target should have: σ as high as possible, in order to reduce the electrical resistance of the target and to amplify the eddy current induction; μ as low as possible, in order to reduce the magnetic reluctance that operates in opposite direction with respect to the eddy currents. Ferromagnetic materials are not recommended as target for ECS system [58] to avoid a mixture of eddy current effect and magnetic reluctance that may cancel each other, hence resulting in a poor net sensitivity.

In general, non-ferromagnetic materials, such as copper, aluminum or stainless steel are preferred as target materials.

However, existing solutions use ferromagnetic materials as a core for the sensor coil, in order to increase the inductance of the coil (Q factor) resulting in high sensitivity. The main limitation is related to the thermal instability that can limit the precision in uncontrolled environments.

4.2.2   Transformer Model of ECS

The coil-target air coupling can be considered as an equivalent transformer[59], as shown in Figure IV.7d. The primary of the transformer, in which the driving current I_1 flows, is comprised of the

inductor L_c and the series resistor R_c, and represents the sensor coil. The secondary of the transformer in which the eddy current I_2 flows, and formed by the inductor L_t and a series resistor R_t in short, represents the target.

According to (25) the equivalent impedance Z_x at the input of the transformer, can be obtained applying the Kirchhoff's Law, KL. The equivalent inductance L_x and series resistance R_x forming Z_x, are given by

$$R_x = R_c + \frac{(\omega M)^2}{R_t{}^2 + (\omega L_t)^2} R_t \qquad (26)$$

$$L_x = L_c - \frac{(\omega M)^2}{R_t{}^2 + (\omega L_t)^2} L_t \qquad (27)$$

Where $\omega = 2\pi f$, being f the frequency of the excitation signal; and M is the mutual inductance between the coil and the target given by

$$M = k(x)\sqrt{L_t L_c} \qquad (28)$$

k is the coupling factor between the primary and the secondary of the transformer, which is a function of the distance x and limited between 0 and 1.

The change in R_x and L_x are highly nonlinear over a large displacement range. If the application requires a small displacement range, an acceptable Z_x-x linearity can be obtained.

ECS requires an AC signal to generate alternating magnetic field. The typical approach is to drive the LC-tank oscillator, comprised of the self-inductance of the coil and the external capacitance. An active circuit acts as a negative resistance restoring the power loss in the tank due to the change in R_x as result of the displacement variations.

4.2.3   Negative resistance perspective

In order to compensate for the tank loss, accounted to R_x, an equivalent negative resistance is needed. The idea is to create an active device that behaves as a negative resistance generator as shown in Figure IV.8a. In steady–state condition the power losses in the tank (due to conductance $G_x=1/R_x$) are counter-balanced by the power drawn from the active device through its negative conductance $-G_m$. In steady-state condition, the circuit will operate in a stable point with a fixed oscillation amplitude. Intuitively we can see that if the G_x become larger than G_m the circuit has net loss and the oscillation amplitude tend to decrease.

(a)   (b)   (c)
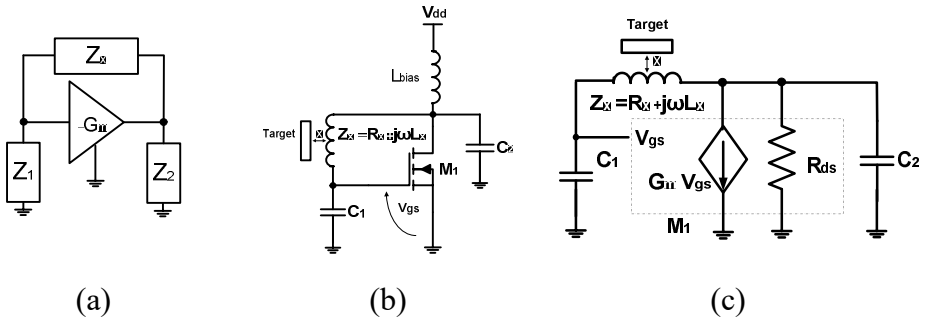
Figure IV.8 a) General LC-tank oscillator schematic; b) Pierce oscillator; c) Small signal circuit for the circuit in (b).

The negative resistance can be obtained by considering the Pierce oscillator configuration as depicted in Figure IV.8b. The circuit is comprised of an active device M_1, a passive network Z_x, the capacitances C_1 and C_2 and the inductor L_{bias} for biasing the circuit. L_{bias} acts as a constant source. Considering the equivalent small signal circuit depicted in Figure IV.8c and applying the KL we can obtain the following equation

$$-G_m \frac{1}{j\omega C_1} + \frac{R_{ds}}{1 + j\omega R_{ds} C_2}$$
$$= \frac{1}{j\omega C_1} + \frac{R_{ds}}{1 + j\omega R_{ds} C_2} + R_x + j\omega L_x \tag{29}$$

In order to trigger an oscillation the two Barkausen criteria conditions must be satisfied. Solving the equation in terms of s=jω we obtain

$$\omega^2 = \frac{C_1 R_x + R_{ds}(C_2 + C_1)}{C_2 C_1 L_x R_{ds}} \tag{30}$$

$$G_m > \frac{C_1}{C_2}\left(\frac{R_x + R_{ds}}{R_{ds}^2}\right) + \frac{C_1}{L_2}\frac{R_x{}^2}{R_{ds}} + \frac{R_x}{L_2}(C_2 + C_1) \tag{31}$$

As denoted in the latter equation the trans-conductance depends on R_x.
By neglecting the term R_{DS} the two above equations become:

$$\omega^2 = \frac{1}{\frac{C_2 C_1}{(C_2 + C_1)} L_x} \tag{32}$$

$$G_m > \frac{R_x}{L_2}(C_2 + C_1) \tag{33}$$

The equation (33) describes the condition on the transconductance of M_1 to ensure the oscillation. Better performance in term of power consumption and sensitivity can be achieved by lowering the R_x and consequently by increasing the quality factor of the coil, which is defined as

$$Q(x) = \frac{\omega L_x}{R_x} \tag{34}$$

The Q factor depends on the displacement, x, because both L_x and R_x are functions of the displacement x. High Q leads to high accuracy and stability. Also the oscillation frequency depends on the x according to Equation(30). By reducing x, the oscillation increases with a lower rate with respect to the decrease of the inductance and consequently the Q decreases.

Thanks to the AC driving signal an electro-magnetic field is created around the inductor L_c, which produce the sensing field. Once the metal target enters the sensing field, eddy currents are induced on its the metal surface. This causes the oscillation amplitude to decrease, the closer it moves to the sensor coil. In other words the amplitude of oscillation dampens until the oscillation will eventually stall. Conversely as the metal object moves away from the sensor the oscillation amplitude increases its intensity.

To extract the displacement information from the measurement a variety of demodulation techniques have been developed for ECS system [55]-[58] e.g. frequency modulation (FM), amplitude modulation (AM), phase detection and balanced bridge.

The purpose of this work is to demonstrate the possibility of obtaining an ultra-low-power and voltage ECS. Thus, the attention is not addressed to the data-extraction technique but rather on the possibility to have an output voltage proportional to the displacement position, x. In this perspective the simplest peak-detector is connected at the gate terminal of the mosfet as shown in Figure IV.9 for the oscillation amplitude

demodulation.
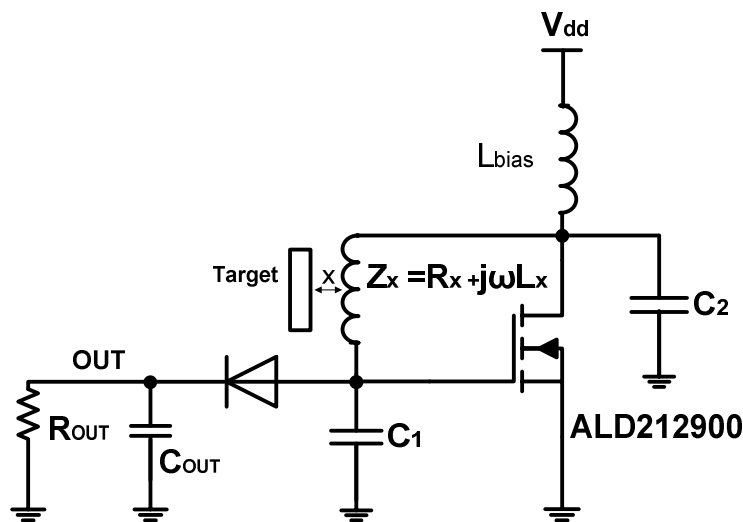
Figure IV.9 Implemented eddy current sensor inteface

Relying on the previous analysis and after a simulation-aided design optimization, the oscillator circuit has been designed and realized using a zero threshold mosfet ALD212900 and high quality passive devices as following described. The ALD212900, with a high forward transconductance and output conductance at very low supply voltages, allows lowering the voltage supply level of the circuit, consequently reducing the power consumption of the circuit. The inductor chosen as L_x (22R106C Murata) has a high Q (beyond 140) at the circuit oscillation frequency (about 160kHz). To ensure the validity of Eq.(31) the terms C_1/C_2 and C_1+C_2 must be minimized. Thus, C_1=10nF is chosen to be lower than C_2=100pF and sized larger than the gate-source capacitance of the mosfet (about 30pF) in order to be unaffected by the variations of the

input capacitance of the mosfet (that depends on its working region).

Conversely to the traditional design of a Pierce oscillator, the oscillator outputted node is taken at the gate of the transistor. The output load is composed by R_{OUT}=886kΩ and C_{OUT}=100nF.

4.2.4   Measurements and results

All the tests have been conducted maintaining constant the operating temperature (T_{amb} = 25°C) in order to eliminate the thermal drift issues. The material used for the target is copper with an area of 15x15mm^2 larger than the diameter of the inductor used as coil. The tests have been conducted by moving the target with respect the coil and by using a micrometric positioning stage.

Figure IV.10 shows the V_{OUT} over time for a dynamic micrometric-displacement of the target with respect to the coil. The circuit is powered by an input voltage of 100mV. In particular the figure shows how the V_{OUT} changes in function of different displacements. Different relative positioning steps (0-500-1000-2000-3000-4000-5000µm) are reported to demonstrate the effective change of V_{OUT}. As previously discussed, when the target is close to the coil, the oscillation amplitude decreases due to the higher power losses, with a consequent decrease of V_{OUT}. Conversely, by moving the target away from the coil the V_{OUT} increases.

(a)   (b)
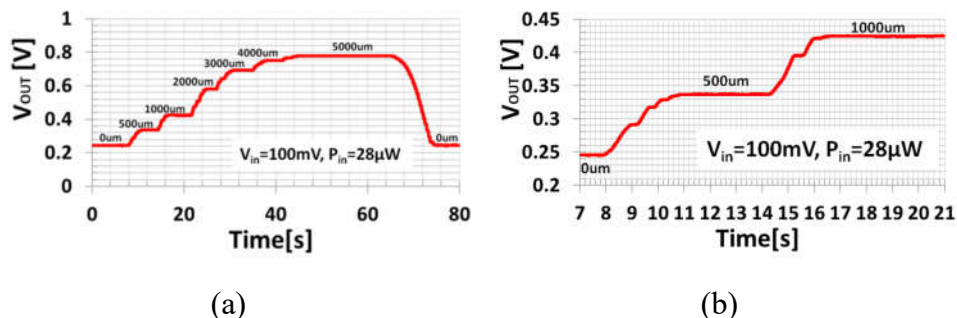
Figure IV.10 a) V_{OUT} over the whole acquisition time during micrometric movements of the target with respet the coil; b) inset of figure (a).

The sensitivity and resolution with reference to [60] are reported in Figure IV.11. Both the sensitivity, S, and the resolution, R, are obtained by discretizing the whole measure range ΔX in *n* sub-ranges:

$$S = \frac{\Delta V_n}{\Delta x_n} = \left[\frac{mV}{um}\right] \tag{35}$$

$$R = \frac{N_n}{S} = [um] \tag{36}$$

where N_n is the RMS voltage noise of the signal [mV] in the n-th sub-range, ΔV_n is the output voltage variation [mV]in the n-th sub-range and Δx_n is the considered sub-range [μm]. The larger the sensitivity, the better is the resolution of the ECS. With a power consumption of only 28uW, the resolution is better than 10μm over a distance range from 0 to 3mm. Specifically, in a the displacement range Δx_n = 0-500μm and with 100mV-supply voltage the resolution can slightly improve to 6um.
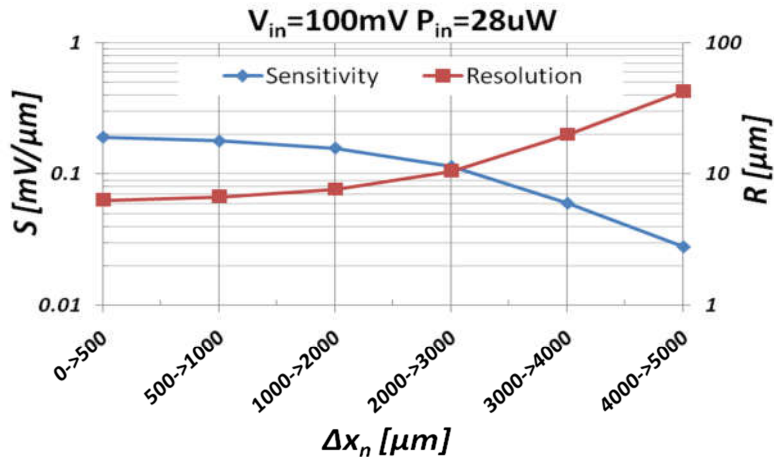
Figure IV.11 Voltage-referred Sensitivity and the Resolution with respect to the Δx_n for the proposed circuit powered by 100mV.

In Figure IV.12 the resolution is analyzed according to different supply voltages. Under equivalent displacement conditions Δx_n, an increase of the supplied voltage, hence of the supplied power, improves the achievable resolution. Specifically, in the displacement range $\Delta x_n = 0$-500μm and with 200mV-supply voltage and 140μW-power consumption the resolution can slightly improve to 3um.

For Δx_n=0-500μm an acceptable linearity R-P_{IN} can be achieved in the supply voltage range 100mV-200mV.
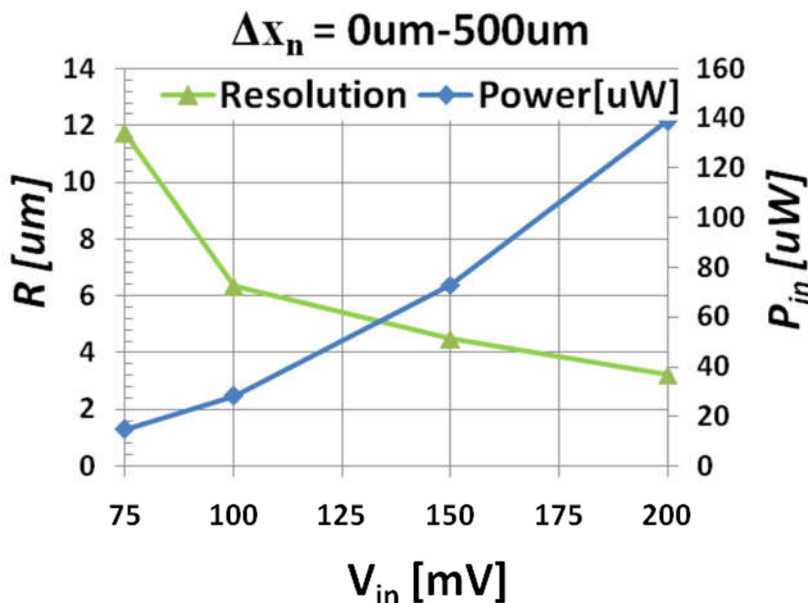
Figure IV.12 Input Power and Resolution according to different supply voltage values into the range 0-500um.

4.2.5 Conclusions

The first ultra-low voltage and power displacement sensor based on the eddy current principle has been presented. The sensor is excited by an ad-hoc designed Pierce oscillator exploiting the high transconductance and output conductance at low level voltages allowed by the ALD212900 (Advanced Linear Device EPAD® MOSFET Family).

The effectiveness of the proposed solution is demonstrated by means of laboratory experiments, which show that resolution of 6μm can be obtained with an input voltage of 100mV and a power consumption of 28uW.

Chapter V
Conclusions

This thesis presents the main research activities carried out by the author during his three years of Ph. D Course of the International Doctorate School in Information and Communication Technologies of the "Università degli Studi di Modena e Reggio Emilia".

In particular, the research activity conducted by the author is threefold.

The first one concerns the investigation of triboelectricity as both new transduction mechanism to harvest energy from vibration and impacts, and new sensor mechanism for low cost flowmeter sensors occurring in many industrial applications.

The second one is related to the design and realization of ultra-low voltage DC-DC converter for Thermal Energy Harvesting (EH) applications.

The third one concerns the design and realization of an ultra-low voltage and power displacement sensor based on eddy current effect.

The first activities have been focused on the development of a Contact-Mode TriboElectric Device (CM-TEDs) whose operating principle is based on the combination of contact electrification and electrostatic induction. The triboelectric device, validated experimental data measured on prototypes fabricated at our premises, generates up to 25µW when subjected to repetitive shocks of 10N intensity. The prototype consists of extremely low-cost commercial silicone used as dielectric material. In

order to maximize the device performance, a simulation-aided custom design has been developed. Differently from the models presented in the literature, the proposed one takes into account the effect of the impact force. This eventually allows us to predict the electrical performances of the device including their dependence on the impact force, thereby overcoming the limits of the classic models. In addition the presented results demonstrate how also the impact force influences the surface charge density, σ, of tribo-electric layers. Several prototypes of ultra-low cost silicone-based CM-TED has been realized to validate the model. The very good agreement between measurements and simulation results confirms that the developed model can predict the output voltage and the output power at given working conditions (e.g. estimated impact force, displacement, electrical load), and can be used to design CM-TEDs for energy harvesting purposes.

The above developed CM-TEDs was used to realize an autonomous ultra-low cost transducer capable of measuring the flow rate of gases and fluids, and which exploits the triboelectric effect to power the sensor. The realized device is extremely low cost because it uses commercial silicone as triboelectric material. The comparison between the performance of a commercial flowmeter and our prototype, demonstrates the effectiveness of the proposed solution in both constant- and variable-flow conditions.

In addition to energy harvesting methods that exploit mechanical energy, the candidate has worked also on the development of energy harvesting systems based on the Seebeck effect and the temperature differences to generate an electrical energy. The voltage and the power generated by the thermoelectric generators (TEGs) are proportional to the

temperature gradient between the hot and the cold junctions and by the Seebeck coefficient of the two thermoelectric materials. The commercial TEGs can generate voltages above 20mV by exploiting thermal gradient lower than 2°C. Large thermal gradients are necessary to produce voltage and power levels suitable for practical applications, e.g. for powering a sensor node. Some recent publications have reported TEG-based applications operating at supply voltages as low as 20 mV but the presented DC-DC converters require specific startup conditions (e.g. use of backup battery at device start-up). The start-up of DC-DC converters requires a time-varying signal, which is commonly obtained from an electronic oscillator. The state-of-the-art commercial devices, instead, rely on low-voltage oscillators operating at minimum 20 mV. This imposes a severe limitation to the maximum energy that can be harvested. The loss of energy conversion for lower voltages (below 20mV) results in a considerable limitation of the application range. To address this issue, the research activity has focused on the possibility to overcome this low-voltage start-up limitation in order to reduce the minimum voltage threshold necessary to enable the startup of the converter. In order to achieve this result, a modification of the typical Armstrong oscillator topologies was realized. After a simulation-aided design optimization, a new DC-DC converter with an 11mV start-up threshold has been developed and realized. The converter can charge a completely discharged 500uF capacitor above 2.1V in 524s starting from 11mV input-voltage. The new circuit is able to convert the voltage generated by the TEG subjected to a very low thermal gradient as low as 0.6°C.

Finally, a Pierce oscillator topology designed to turn on with low-

supply voltage has been used for the realization of ultra-low voltage and power proximity sensors based on eddy current effect. Differently from the circuit presented in the literature, the proposed one aims to demonstrate micrometric-resolution low-power eddy current displacement sensor. The developed sensor has a resolution slightly higher than 6um with a power consumption lower than 30uW. It represents the first one low-power eddy current displacement sensor.

Acknowledgments

First, I would like to thank my advisor Prof. Paolo Pavan and Co-tutor prof. Luca Larcher for his support and guidance throughout the Ph. D. Course.

A special thank goes to Ing. Alessandro Bertacchini for his mentorship and also for the continuous sharing of opinions, who made my Ph. D, citing his words, "a school of life". Another thank goes to Gabriele for having wanted to create IndioTECH.

I sincerely thank my family: my parents Fausto and Mariagrazia, my grandmothers Pina and Rosa and my brother Matteo for the continuous confidence and support.

I sincerely thank my cavaz-friends.

Last, but obviously not least, I thank my beloved wife Elisabetta for having wanted to share His life with me.

The rest is history.

References

[1] Texas Instruments. (2010) Energy Harvesting - ULP meets energy harvesting: A game-changing combination for design engineers. [Online]. http://www.ti.com/lit/wp/slyy018a/slyy018a.pdf

[2] Tom J. Kazmierski and S. Bebby, *Energy Harvesting Systems - Principles, Modeling and Applications*.: Springer.

[3] Scorcioni S., Bertacchini A., Dondi D., Larcher L., Pavan P., Mainardi G., "A vibration-powered wireless system to enhance safety in agricultural machinery," In Proceedings of IECON 2011 - 37th Annual Conference on IEEE Industrial Electronics Society, Melbourne, Australia, 7-10 Nov. 2011, vol., no., pp.3510-3515

[4] Kim, Sang-Gook, Shashank Priya, and Isaku Kanno. "Piezoelectric MEMS for Energy Harvesting." MRS Bulletin 37.11 (2012): 1039–1050. Web.© Materials Research Society 2012

[5] Jun Chen and Zhong Lin Wang "Reviving Vibration Energy Harvesting and Self-Powered Sensing by a Triboelectric Nanogenerator", Joule 1, 480–521, November 15, 2017

[6] Bertacchini, L. Larcher, M. Lasagni and P. Pavan, "Ultra low cost triboelectric energy harvesting solutions for embedded sensor systems," *in Proc. IEEE-NANO*, 2015, pp. 1151-1154.

[7] Marco Lasagni, Paolo Pavan, Alessandro Bertacchini, Luca Larcher "Force Impact Effect in Contact-Mode Triboelectric Energy Harvesters: Characterization and Modeling", IEEE Sensors 2016 Conference, Orlando.

[8] Lingen Chen, Jianzheng Gong, Fengrui Sun, Chih Wu, "Effect of heat transfer on the performance of thermoelectric generators", Int. J. Therm. Sci. 41 (2002) 95–99

[9] W. Chen, C.Wang , C. Hung, "Geometric effect on cooling power and performance of an integrated thermoelectric generation-cooling system", Energy Conversion and Management 87 (2014) 566–575.

[10]   D.Mitrani, J.A. Tome, J. Salazar, A. Two, M. J. Garcia, J.A. Chavez , "Methodology for Extracting Thermoelectric Module Parameters", IMTC 2004- Instrumentation and Measurement Technology Conference, Como, Italy, 18-20 May 2004

[11]   Vullers R.J.M., R. Van Schaijk, I. Doms, C. Van Hoof, and R. Mertens, "Micropower energy harvesting," Solid-State Electronics, vol. 53, no. 7, pp. 684-693, July 2009.

[12]   https://www.lairdtech.com/support/learning-center/product-selection-tools/aztec-software-download

[13]   LTC3108 www.linear.com/LTC3108, " Ultralow Voltage Step-Up Converter and Power Manager"

[14]   SimiaoNiu, Sihong Wang, Long Lin, Ying Liu, Yu Sheng Zhou, Youfan Hu and Zhong Lin Wang, "Theoretical study of contact-mode triboelectric nanogenerators as an effective power source", Energy and Environmental Sciences, 2013.

[15]   Zhong Lin Wang, "Triboelectric Nanogenerators as NewEnergy Technology for Self-PoweredSystems and as Active

Mechanical andChemical Sensors".

[16]   Logan S. McCarty and George M. Whitesides, "Electrostatic Charging Due to Separation of Ions at Interface: Contact eletrification of Ionic Electrets", Angew.Chem.Int, Ed 2008, 47, 2188-2207.

[17]   Eugen. R.Neagu and Carlos. J.Dias, "Charge injection/extraction at a Metal-dielectric interface: experimental validation" *IEEE Eectrical Insulation Magazine,* pp. 15-22, January/February 2009.

[18]   Horn R.G, Smith D.T, "Contact electrification and adhesion between dissimilar material" , Science 1992, 362-364.

[19]   Mario M.Apodaca, Paul J.Wesson,KyleJ.M.Bishop, Mark A.Ratner, and BartoszA.Grzybowski, "Contact eletrification between identical materials" , Angew.Chem.Int,Ed 2010,49,946-949.

[20]   LokeshDhakar, F E H Tay, and Chengkuo Lee, "Investigation of contact electrification based broadband energy harvesting mechanism using PDMS microstructures", Journal of Micromechanism and Microengineering,vol 24.

[21]   S. Niu, S. Wang, L. Lin, Y. Liu, Y. Sheng Zhou, Y. Hua, Z.L. Wang "Theoretical study of contact-mode triboelectric nanogenerators as an effective power source" *Energy Environ. Sci.,* vol. 6, pp 3576-3583, 2013.

[22]   L. Dhakar, F. E. H. Tay and C. Lee, "Development of a Broadband Triboelectric Energy Harvester With SU-8

Micropillars," in Journal of Microelectromechanical Systems, vol. 24, no. 1, pp. 91-99, Feb. 2015.

[23]   T. Chen, Y. Xia, W. Liu, H. Liu, L. Sun and C. Lee, "A Hybrid Flapping-Blade Wind Energy Harvester Based on Vortex Shedding Effect," *in J. Microelectromech. Syst*, vol. 25, no. 5, pp. 845-847, Oct. 2016.

[24]   Y. Xia, J. Zhou, T. Chen, H. Liu, W. Liu, Z. Yang, P. Wang and L. Sun, "A hybrid flapping-leaf microgenerator for harvesting wind-flow energy," *in Proc. IEEE MEMS*, Shanghai, 2016, pp. 1224-1227.

[25]   J. Park, K. S. Yun, "Hybrid energy harvester based on piezoelectric and triboelectric effects" *in Proc IEEE MEMS*, Shanghai, 2016, pp. 41-42.

[26]   L. Dhakar, F. E. H.Tay and C. Lee, "Investigation of contact electrification based broadband energy harvesting mechanism using elastic PDMS microstructures", *in J. Micromech and Microeng*, vol. 24, pp. 1-11, 2014.

[27]   M. Seol, J. Han, S. Park, S. Jeon, Y. Choi, "Hybrid energy harvester with simultaneous triboelectric and electromagnetic generation from an embedded floating oscillator in a single package" *Nano Energy*, Vol. 23, pp. 50-59, May 2016.

[28]   L. Dhakar, S. Gudla, et al. "Large Scale Triboelectric Nanogenerator and Self-Powered Pressure Sensor Array Using Low Cost Roll-to-Roll UV Embossing", *Nature Scientific Reports*, 2016,6,22253.

[29]   X. Cheng, Y. Song, M. Han, B. Meng, Z. Su, L. Miao, H. Zhang, "A flexible large-area triboelectric generator by low-cost roll-to-roll process for location-based monitoring", *Sens. and Actuat. A: Phys*, Vol. 247, Aug 2016, pp. 206-214.

[30]   X. Cheng, B. Meng, M. Han, M. Shi and H. Zhang, "Floor-based large-area triboelectric generator for active security monitoring," *in Proc IEEE ICCE*, Las Vegas, NV, 2015, pp. 581-582.

[31]   M. S. Rasel, M. A. Halim and J. Y. Park, "A PDMS based triboelectric energy harvester as self-powered, active tactile sensor system for human skin," *In Proc. IEEE SENSORS*, 2015, pp. 1-4.

[32]   F. A. Hassani and C. Lee, "A Triboelectric Energy Harvester Using Low-Cost, Flexible, and Biocompatible Ethylene Vinyl Acetate (EVA)", *in J. Microelectromech. Syst*, vol. 24, no. 5, pp. 1338-1345, Oct. 2015.

[33]   Y.Su et al., "Fully enclosed cylindrical single-electrode-based triboelectric nanogenerator," *ACS Appl. Mater. Interf.*, vol. 6, no. 1, pp. 553–559, 2014.

[34]   M.L. Seol, J.-H. Woo, D.-I. Lee, H. Im, J. Hur, and Y.-K. Coi, "Nature-replicated nano-in-micro structures for triboelectric energy harvesting," *Small*, vol. 10, no. 19, pp. 3887–3894, 2014.

[35]   M. L. Seol, J.-Woo Han, J. H. Woo, Dong-Il Moon, Jee-Yeon Kim and Y. K. Choi, "Comprehensive analysis of deformation of interfacial micro-nano structure by applied force in triboelectric energy harvester," *in Proc. IEEE IEDM*, 2014, pp.

8.3.1-8.3.4.

[36]   D. Hong, Y. M. Choi and J. Jeong, "The quantitative analysis for a contact-mode triboelectric energy harvesting device," *In Proc. IEEE AIM*, 2015, pp. 563-566.

[37]   S. Matsusaka, H. Maruyama, T. Matsuyama, M. Ghadiri, "Triboelectric charging of powders: A review", Chem. Eng. Sci., Vol. 65, Issue 22, pp 5781-5807, 2010.

[38]   Y. Zi, C. Wu, W. Ding, Z.L. Wang, "Maximized Effective Energy Output of Contact-Separation-Triggered Triboelectric Nanogenerators as Limited by Air Breakdown", Adv. Funct. Mater, 1616-3028, DOI: 10.1002/adfm.201700049, May. 2017.

[39]   David Salerno, "Ultralow Voltage Energy Harvester Uses Thermoelectric Generator for Battery-Free Wireless Sensors", LT Journal of Analog Innovation, vol. 20,no 3.

[40]   Y.K. The and P. K. T. Mok, "Design of transformer-based boost converter with 21mV self-start-up voltage and 74% power efficiency", IEEE J. Solid-staet Circuits, vol. 49, no, 11, Nov 2014, pp. 2694-2704.

[41]   J. P. et al, "A 40mV transformer-reuse self-startup boost converter with MPPT control for thermoelectric energy harvesting", IEEE J. Solid-State Circuits, vol. 47, no. 12, Dec. 2012, pp. 3055-3067.

[42]   K.Z. Ahmed and S. Mukhopadhyay, "A wide conversion ratio, extended input 3.5uA boost regulator with 82% efficiency for low-voltage energy harvesting", IEEE trans. Power electron,

vol. 29, no 9 . Sept 2014, pp. 4776-4786.

[43]   J. P .Im, S. Moon and C. Lyuh , "Transformer- reuse reconfigurable synchronous boost converter with 20mV MPPT-input, 88% efficiency and 37mW maximum output power", ETRI journal. vol. 38 no. 4th August 2016

[44]   A. Chini, "Analysis of self-oscillating switched-mode Circuit for low-voltage energy harvesting", Electronic Letters Vol.49, no 15, 18th July 2013.

[45]   Infineon,   Mosfet   BSP149.[online]. https://www.infineon.com/dgdl/Infineon-BSP149-DS-v02_01-en.pdf?fileId=db3a30433c1a8752013c1fcbb815397c

[46]   [1]   S. Subramanian and U. Kumar, "Augmenting numerical stability of the Galerkin finite element formulation for electromagnetic flowmeter analysis," inIET Science, Measurement & Technology, vol. 10, no. 4, pp. 288-295, 7 2016.

[47]   [2]   Hu, D. Zheng and S. Fan, "Experimental Study and Implementation of a Novel Digital Closed-Loop Control System for Coriolis Mass Flowmeter," inIEEE Sensors Journal, vol. 13, no. 8, pp. 3032-3038, Aug. 2013.

[48]   [3]   L. Shao, K. J. Xu and Z. P. Shu, "Segmented Kalman Filter Based Antistrong Transient Impact Method for Vortex Flowmeter," inIEEE Transactions on Instrumentation and Measurement, vol. 66, no. 1, pp. 93-103, Jan. 2017.

[49]   [4]   W. Fernandes, M. D. Bellar and M. M. Werneck, "Cross-Correlation-Based   Optical   Flowmeter,"   inIEEE

Transactions on Instrumentation and Measurement, vol. 59, no. 4, pp. 840-846, April 2010.

[50]　　[5]　　H. Zhao, L. Peng, T. Takahashi, T. Hayashi, K. Shimizu and T. Yamamoto, "CFD-Aided Investigation of Sound Path Position and Orientation for a Dual-Path Ultrasonic Flowmeter With Square Pipe," in IEEE Sensors Journal, vol. 15, no. 1, pp. 128-137, Jan. 2015.

[51]　　[6]　　D. Zheng, J. Mei and M. Wang, "Improvement of gas ultrasonic flowmeter measurement non-linearity based on ray tracing method," inIET Science, Measurement & Technology, vol. 10, no. 6, pp. 602-606, Sept 2016.

[52]　　[7]　　T. Jiang, X. Chen, K. Yang, C. Han, W. Tang and Z. L. Wang, "Theoretical study on rotary-sliding disk triboelectric nanogenerators in contact and non-contact modes" in Nano Research, vol. 9, no. 4, pp. 1057-1070, April 2016.

[53]　　[8]　　L. Lin, S. Wang, S. Niu, C. Liu, Y. Xie and Z. L. Wang, "Noncontact Free-Rotating Disk Triboelectric Nanogenerator as a Sustainable Energy Harvester and Self-Powered Mechanical Sensor" in ACS Applied Materials & Interfaces, vol.6, no. 4, pp. 3031-3038, 2014.

[54]　　S.N. Nihtianov and G.C. Meijer "Application challenges of capacitive sensors with floating targets" AFRICON, 2011, pp 1-6.

[55]　　M. R. Nabavi, and S. Nihtianov, "Eddy-current sensor interface for advanced industrial applications," Industrial Electronics, IEEE Transactions on, vol. 58, no. 9, pp. 4414-4423,

2011.

[56]   M. R. Nabavi, M. A. P. Pertijs and S. Nihtianov, "An interface for eddy-current displacement sensors with 15-bit resolution and 20mHz excitation" IEEE Journal of Solid-State Circuits, vol. 48, No 11, November 2013.

[57]   Wang, H., Liu, Y., Li, W., & Feng, Z. (2014, October). "Design of ultrastable and high resolution eddy-current displacement sensor system". InIndustrial Electronics Society, IECON 2014-40th Annual Conference of the IEEE (pp. 2333-2339). IEEE.

[58]   S. D. Welsby, and T. Hitz, "True position measurement with eddy current technology," Sensors-the Journal of Applied Sensing Technology, vol. 14, no. 11, pp. 30-41, 1997.

[59]   G.Y.Tian,Z.X.Zhao,andR.W.Baines,"Theresearchofinhom ogeneity ineddycurrentsensors,"Sens.   Actuators   A, Phys.,vol.69,no.2,pp.148– 151, Aug. 1998.

[60]   Doll J.C., Pruitt B.L. (2013) "Sensitivity, Noise and Resolution. In: Piezoresistor Design and Applications", Microsystems and Nanosystems, vol 1. Springer, New York, NY